

UNIVERSITY of CALIFORNIA
SANTA CRUZ

**A THREE STREAM OCEAN OPTICS MODEL: REGIONAL
IMPLEMENTATION AND VALIDATION**

A thesis submitted in partial satisfaction of the
requirements for the degree of

MASTER OF SCIENCE

in

SCIENTIFIC COMPUTING AND APPLIED MATHEMATICS

by

Miles Miller

December 2022

The Thesis of Miles D. Miller is approved:

Professor Christopher A. Edwards, Chair

Professor Pascale Garaud

Professor Daniele Venturi

Peter Biehl
Vice Provost and Dean of Graduate Studies

Copyright © by

Miles Miller

2022

Contents

List of Figures	vi
List of Tables	viii
Abstract	viii
Dedication	x
Acknowledgements	xi
1 Introduction	1
2 Optical Model	4
2.0.1 Three Stream Model	6
2.0.2 Two Stream Model	11
2.1 Solving Three Stream Equations	11
2.1.1 Analytical Solution	12
2.1.2 Numerical Solutions	14
2.2 Estimating R_{rs} from Simulated Irradiance	22
2.3 Normalized and Directional Surface Irradiance	23
2.4 OCx Chlorophyll-a Ocean Color Algorithm	26

3	Validation of the Optical Model	29
3.1	CalCOFI and CCI Validation	31
3.1.1	Data Acquisition	32
3.1.2	Implementing the Optical Model	32
3.1.3	R_{rs} Correlation	34
3.1.4	Chlorophyll-a Correlation	36
3.1.5	Summary	42
3.2	OOI Surface Piercing Profiler Validation	43
3.2.1	Data Acquisition	43
3.2.2	Absorption and Scattering	44
3.2.3	Spectral Irradiance	49
4	Conclusions	54
4.1	Moving forward	56

List of Figures

2.1 Three Stream Visualization	5
2.2 Coefficients of Absorption and Scattering	9
2.3 Analytical Three Stream Solution	13
2.4 Three Stream Solution	17
2.5 Resolution Sensitivity	21
2.6 Directional Irradiance Sensitivity	24
2.7 OCx Algorithm	26
3.1 Application of Optical Model to Biogeochemical Model	29
3.2 CalCOFI Cast Locations	31
3.3 Synechococcus R_{rs} Correlation	33
3.4 R_{rs} Correlation Statistics	35
3.5 OCx Using CCI R_{rs} Compared to CCI Chlorophyll-a	37
3.6 Model Compared to CalCOFI Chlorophyll-a	38
3.7 Chlorophyll-a Correlation Statistics	39
3.8 Model Compared to CCI Chlorophyll-a	40
3.9 CCI Compared to CalCOFI Chlorophyll-a	41
3.10 OOI Spectral Absorption and Modeled	45

3.11 OOI Spectral Absorption and Modeled Using Improved CDOM . . .	47
3.12 Model Using a_{OOI} and b_{OOI} Compared to OOI SPKIR Downward Irradiance	49
3.13 Model Compared to OOI Downward Irradiance Phy Types	51
3.14 Deployment Time Series of Downward Irradiance Bias	52

List of Tables

2.1 Optical Constants	8
2.2 Phytoplankton Equivalent Spherical Diameter	10
2.3 OCx Coefficients	27
3.1 CCI and CalCOFI Model CDOM Sensitivity Results	48

Abstract

A Three Stream Ocean Optics Model: Regional Implementation and Validation

by

Miles Miller

A three stream irradiance model is implemented and tested to determine its utility for biogeochemical data assimilation of remote sensing reflectance, $R_{rs}(\lambda)$, data in the California Current System. Two different numerical methods were tested to solve the model, but the shooting method using a 4th order classical Runge Kutta scheme was implemented. The optical model solves for $R_{rs}(\lambda)$ from the concentrations of variable optical constituents and their respective wavelength dependent light scattering and absorption properties. Using single phytoplankton type absorption and scattering estimates, the optical model produces R_{rs} values that correlate to satellite observed R_{rs} more closely for certain phytoplankton types than others. The model produced accurate downward irradiance fields when using observed absorption and scattering profiles obtained from the Ocean Observatories Initiative's Oregon Shelf Surface Piercing Profiler Mooring. Through this forward modeling based comparison to observations it was found that the optical model can produce accurate profiles under certain conditions, making it promising for data assimilation of R_{rs} , but outstanding issues remain to be addressed, including accurately resolving community structure, improvements to the parametrization of constituents other than phytoplankton, and atmospheric influence on surface boundary conditions.

To my advisor,

Christopher A. Edwards

Acknowledgements

I would like to express my sincerest gratitude to my advisor Christopher Edwards. Throughout my research and time at UCSC, he has instilled indispensable knowledge in me and given me the courage to approach difficult problems with an open mind and determination. I will always be thankful for his guidance, motivation, and kindness. Thank you Chris. I would like to thank my committee, Pascale Garaud and Daniele Venturi, for their advice and patience in my writing of this thesis as well as their support throughout my academic career. I would also like to thank project collaborator Jonathan Izett for being there every step of the way to throughout this project and my graduate experience. I am grateful for his advice, ocean modeling expertise, and help through my many academic and research challenges. This project would not be possible without the critical motivation and direction of John Wilkin at Rutgers University. Also, I would like to express my appreciation to Stephanie Dutkiewicz for her advice, inspiration, and sharing of important algorithmic data. Furthermore, I would like to thank Shubha Sathyendranath and her team at Plymouth Marine Laboratory for providing key information to approaching optical model discrepancies. The importance of the team at the Ocean Observatories Initiative and their hands-on support to obtaining data can not be understated—specifically, Christopher Wingard, for his help with formulating methods to implement optical data. I would also like to acknowledge the utility of data provided by the California Cooperative Oceanic Fisheries Investigations as well as the Climate Change Initiative. I would like to thank my mom, dad, and little brother for pushing me to achieve my dreams and providing me with the opportunities to do so. This work was made possible with the generous support of

the Simons Foundation (Award 549949).

1

Introduction

Ocean biogeochemical modeling is used to simulate and forecast the evolution and interactions of physical, chemical, and biological constituents in the ocean, which can help to predict the occurrence of important marine events. (Song et al., 2016). Biogeochemical modeling has utility in monitoring ocean ecosystem health, (Fennel et al., 2019), and in understanding effects of global climate changes, (Quére et al., 2005). The accuracy of simulating variable dynamics in biogeochemical models is continually bound by the large numbers of constituents and the complexities of their often non-linear interactions (Baird, 2010). Data assimilation has been shown to improve the correlation between biogeochemical observations and model output through constraint of model trajectory using assimilation to observed data (Edwards et al., 2015).

Current regional assimilation methods in the California Current System (CCS) rely on satellite-derived surface measurements of chlorophyll-a (chl-a) for the assimilation of biological constituents in the Regional Ocean Modeling System (ROMS) using a log-transformed 4D-Var algorithm, see (Song et al., 2016). Satel-

lite chl-a measurements are derived from wavelength dependent remote sensing reflectance data using ocean color chl-a algorithms such as O'Reilly et al. (1998). The use of remote sensing reflectances (R_{rs}) could potentially provide a more direct, adaptable, and broader approach to data assimilation in the California Current System (CCS) over the use of derived chl-a data. The effectiveness of data assimilation using R_{rs} in a marine biogeochemical model of the Great Barrier Reef is shown in Jones et al. (2016).

Assimilation of R_{rs} requires the use of an optical model to solve for R_{rs} from biogeochemical model constituents (Jones et al., 2016). Ocean optics models such as those described by Sathyendranath & Platt (1997), Dutkiewicz et al. (2015), Jones et al. (2016), Baird et al. (2016), Gregg & Rousseaux (2017), or Lee et al. (2002) formulate R_{rs} from the concentrations of variable optically important constituents in the ocean water column and their respective wavelength dependent light scattering and absorption properties. ROMS provides a physical and biogeochemical model framework around which the ocean optics model is built. ROMS biogeochemical dynamics includes the interactions of large and small phytoplankton, large and predator zooplankton, particulate and dissolved organic nitrogen, nitrate, ammonium, silicate, and particulate organic silica. (Kishi et al., 2007) The primary constituents of interest to an optical model include phytoplankton, CDOM, and detritus as well as the effects of pure seawater (Dutkiewicz et al., 2015). Their are differences between the variables that are optically important and those that are biogeochemically important. As a result, accurate parametrization of optical constituents that are not included in the biogeochemical model is a crucial aspect of the optical model formulation.

The work that follows seeks to apply the three-stream irradiance model

described by [Dutkiewicz et al. \(2015\)](#) in the context of its application for data assimilation of R_{rs} in ROMS and the CCS. This analysis includes the evaluation of the numerical methods used to solve the irradiance equations, formulation of constituent parameterizations, comparison of results using in situ data to satellite R_{rs} observations, and model validation against profiled absorption and irradiance data.

2

Optical Model

The basis for an ocean optics model lies in solving the interactions of incident light energy with optically active constituents in the water. In addition to the effects of pure seawater, constituents such as phytoplankton, colored dissolved organic matter (CDOM), and detritus each play important roles in ocean optics and remote sensing (Dutkiewicz et al., 2015). The optical models we explore focus on the absorption and scattering of light in upward and downward directed streams of irradiance in the water column. The scalar valued irradiance ($\text{Wm}^{-2}\text{nm}^{-1}$) streams represent integrals of vector valued radiance ($\text{Wm}^{-2}\text{sr}^{-1}\text{nm}^{-1}$) through different solid angles. Radiance is a function of viewing angle while irradiance is the radiometric flux per unit area (Ryer, 1997). The model takes incident irradiance just below the ocean's surface as input and returns the upwelling component of the light that results from the interactions with the various constituents. Two different irradiance stream based models are explained in greater detail in section 2.0.1 and 2.0.2. The ratio of the upward component to the initially downward directed light is highly sensitive to the spectral absorption and scattering compositions of the liv-

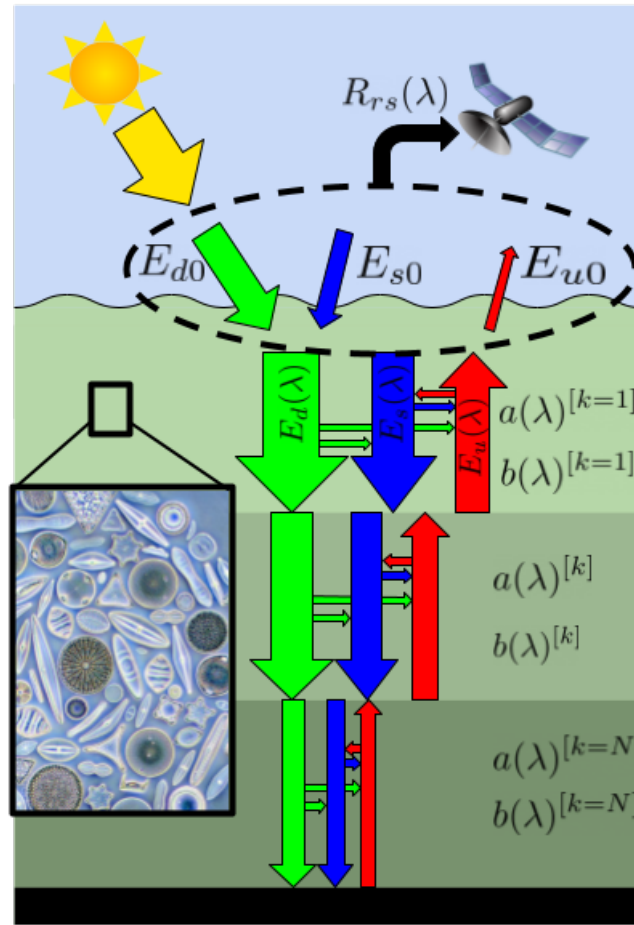


Figure 2.1: The interactions of the three irradiance streams within the absorption and scattering layers of the water column. The green, blue, and red arrows designate the downward direct, downward diffuse, and upwelling streams respectively. The horizontal arrows represent the coupling of the different streams within the layer. The black box shows an example of different phytoplankton constituents. The black, dashed circle demonstrates the formulation of R_{rs} from the surface values of the three irradiance streams.

ing and non-living constituent concentrations. The ratio of downward and upward surface irradiance is then used to formulate R_{rs} that is comparable to R_{rs} observed by satellite.

Finally, R_{rs} can be translated into surface chl-a using algorithms that rely on empirically derived relationships between R_{rs} at different wavelengths and in situ chl-a observations. The optical model can be divided into three main stages: the estimation of absorption and scattering from optically important constituent concentrations and parametrizations, solving the radiative transfer equations for absorption and scattering dependent irradiance fields, and translating resulting irradiance to R_{Rs} and chl-a. The following sections describe the different methods used for each stage.

2.0.1 Three Stream Model

Our three-stream irradiance model is the same as described by [Dutkiewicz et al. \(2015\)](#). The three stream model is composed of two downward irradiance streams (downward direct, $E_d(\lambda, z)$, and downward diffuse, $E_s(\lambda, z)$) and one upward irradiance stream (upwelling, $E_u(\lambda, z)$). Following [Dutkiewicz et al. \(2015\)](#) the three stream irradiance model is written as,

$$\frac{dE_d(\lambda, z)}{dz} = \frac{a(\lambda, z) + b(\lambda, z)}{\bar{\nu}_d} E_d(\lambda, z) \quad (2.1)$$

$$\frac{dE_s(\lambda, z)}{dz} = \frac{a(\lambda, z) + r_s b_b(\lambda, z)}{\bar{\nu}_s} E_s(\lambda, z) - \frac{r_u b_b(\lambda, z)}{\bar{\nu}_u} E_u(\lambda, z) - \frac{b_f(\lambda, z)}{\bar{\nu}_d} E_d(\lambda, z) \quad (2.2)$$

$$\frac{dE_u(\lambda, z)}{dz} = -\frac{a(\lambda, z) + r_u b_b(\lambda, z)}{\bar{\nu}_u} E_u(\lambda, z) + \frac{r_s b_b(\lambda, z)}{\bar{\nu}_s} E_s(\lambda, z) + \frac{b_b(\lambda, z)}{\bar{\nu}_d} E_d(\lambda, z), \quad (2.3)$$

where a and b are the total absorption and scattering of the modeled water column, including both forward b_f and backward b_b scattering. The downward direct irradiance, $E_d(\lambda, z)$ is represented by an independent differential equation (equation [2.1](#)),

with the decay rate with depth directly proportional to its own amplitude and to the sum of the absorption and scattering. In contrast, the downward diffuse and upwelling irradiances, $E_s(\lambda, z)$ and $E_u(\lambda, z)$ respectively, form a coupled, two-point boundary value problem (equations 2.2-2.3). The downward diffuse irradiance decays with depth due to absorption and backscatter of $E_s(\lambda, z)$ specifically (with its forward scattered component remaining within $E_s(\lambda, z)$ to deeper layers); meanwhile, increases in $E_s(z, \lambda)$ with depth result from backscattered upwelling irradiance and forward scattered downward irradiance. Similarly, the upward irradiance decays in the upward direction due to its own absorption and backscattering and increases in the upward direction due to backscattered $E_s(\lambda, z)$ and $E_d(\lambda, z)$. Variables r_s , r_u , and r_d are effective scattering coefficients and $\bar{\nu}_d$, $\bar{\nu}_s$, and $\bar{\nu}_u$ are the average cosines described by Dutkiewicz et al. (2015) with values provided in table 2.1. The effective scattering coefficients represent corrections to the backward scattering and are derived constants following Aas (1987). The three stream equations are derived from the classical radiative transfer equation under the assumption that the ocean is optically isotropic (Dutkiewicz et al., 2015). Figure 2.1 schematically diagrams the interactions between these three streams. Example solutions of the three streams for different phytoplankton profiles are shown in figure 2.3 and figure 2.4. The opposite vertical coordinate construction of Dutkiewicz et al. (2015) is taken, defining z to be negative below the sea surface and decreasing downward.

The total absorption is written as a sum of the absorption due to pure seawater, a_{wat} , shown in figure 2.2a, and the absorption due to the constituents within the water column, including but not limited to the absorption due to phytoplankton, a_{phy} , and colored dissolved organic matter (CDOM), a_{CDOM} . The scattering is the sum of the scattering due to water, b_{wat} , and the scattering due to phytoplankton,

Constant	Value
r_d	1.0
r_s	1.5
r_u	3.0
\bar{v}_d	0.8
\bar{v}_s	0.83
\bar{v}_u	0.4

Table 2.1: The values of constant effective scattering coefficients and average cosines (following Dutkiewicz et al. (2015) and Aas (1987)).

b_{phy} . Other optical models include estimates of absorption and scattering due to detritus (e.g., Dutkiewicz et al. (2015) and Baird et al. (2016)). The total absorption (m^{-1}) and total scattering (m^{-1}) used in the optical model are as follows,

$$a(\lambda) = a_{\text{wat}}(\lambda) + a_{\text{phy}}(\lambda) + a_{\text{cdom}}(\lambda) \quad (2.4)$$

$$b(\lambda) = b_{\text{wat}}(\lambda) + b_{\text{phy}}(\lambda). \quad (2.5)$$

The total absorption and scattering from all phytoplankton types is the sum of the absorption and scattering of each respective type within a given community,

$$a_{\text{phy}} = \sum_i^{N_{\text{phy}}} \alpha_{\text{phy}_i}(\lambda) \rho_{\text{phy}_i}(z) \quad (2.6)$$

$$b_{\text{phy}} = \sum_i^{N_{\text{phy}}} \beta_{\text{phy}_i}(\lambda) \rho_{\text{phy}_i}(z), \quad (2.7)$$

where $\rho(z)$ designates the concentration of the phytoplankton type in units of milligrams of Chla per cubic meter and $\alpha(\lambda)$ and $\beta(\lambda)$ are coefficients that describe the spectrally dependent absorption and scattering (shown in 2.2). Coefficients for dif-

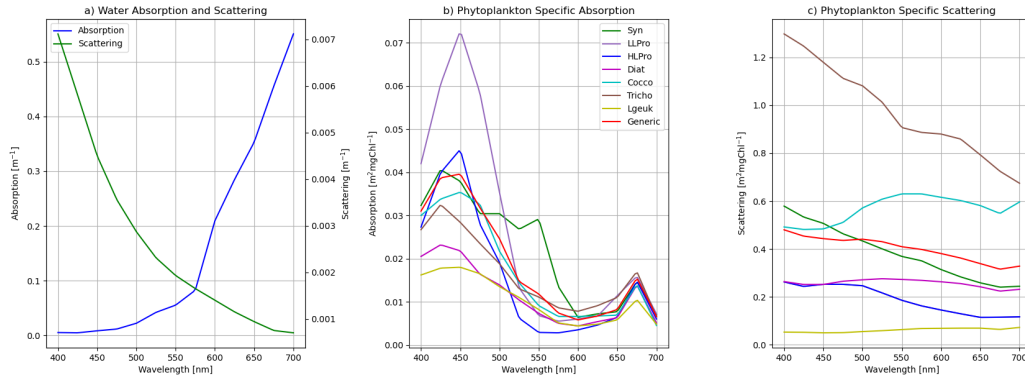


Figure 2.2: a) The absorption and scattering due to pure seawater plot as a function of wavelengths from 400-700 nm. b) The phytoplankton specific absorption coefficient, α , for different wavelengths. Each line corresponds to a species of phytoplankton including synechococcus, low light prochlorococcus, high light prochlorococcus, diatom, coccolithophores, trichodesmium, large eukaryotes, and a 'generic' mean coefficient. c) The phytoplankton specific scattering coefficient, β , for different wavelengths and the same species as previously designated.

ferent phytoplankton types and their spectral dependence are shown in figure 2.2.b and 2.2.c. Backscattering is taken to be a function of phytoplankton type-specific, equivalent spherical diameter (ESD), μm , following Whitmire et al. (2010) as,

$$b_{b\text{phy}} = b_{\text{phy}}(4.390 \times 10^{-3} \times \text{ESD}^{0.432}), \quad (2.8)$$

with the approximate ESD for the different phytoplankton types provided in table 2.2.

Back-scattering has also been estimated in other ways. Morel et al. (2002) estimates back-scattering as a function of chl-a concentration, Dutkiewicz et al. (2015) estimates it from an inversion of observed downwelling irradiance and zenithward radiance, and lastly Baird et al. (2016) as a function of cellular carbon content. The forward scattering is simply, $b_f = b - b_b$. It is assumed that the ratio of backward

Phytoplankton Type	ESD [μm]
HLPPro	0.6
LLPro	0.6
Cocco	4
Diat	17
Generic	10
Syn	0.98
Lgeuk	27.64
Tricho	6.00

Table 2.2: The equivalent spherical diameter (ESD) of the different phytoplankton types.

scattering to forward scattering is constant across wavelengths.

Properly resolving CDOM is of significant importance to accurate light dynamics, “CDOM has been demonstrated to exert primary control on ocean color by its absorption of light energy, which matches or exceeds that of phytoplankton pigments in most cases” (Nelson & Siegel, 2013). Nelson & Siegel (2013) also explains that while CDOM was once thought to have mainly terrestrial influence, recent work has shown that “Autochthonous production dominates the surface ocean signal in the subtropics” (Nelson & Siegel, 2013). Thus an accurate representation of CDOM is important not only for the coastal region, but for the regional deep ocean domain as well. The absorption from CDOM is preliminarily estimated as a function of chlorophyll-a concentration following Stramska & Stramski (2005),

$$a_{\text{CDOM}}(\lambda, z) = 0.012(\text{Chla}(z))^{0.65} e^{-0.014(\lambda-440)}. \quad (2.9)$$

Other approximations to CDOM absorption include parameterizing CDOM concentration as a function of salinity (Baird et al., 2016) and using a CDOM-based reference absorption (Dutkiewicz et al., 2015).

2.0.2 Two Stream Model

The three stream model can also be simplified into a two stream model, composed of one upward and one downward stream. This approach more closely follows the work of Sathyendranath & Platt (1998) and Sathyendranath & Platt (1997), but with coefficients translated to mimic those of Dutkiewicz et al. (2015). Instead of partitioning the downward stream into its diffuse and direct components, the two stream variant of the light model solves the downwelling and upwelling streams to give the following set of two equations,

$$\frac{dE_d}{dz} = \frac{a + b_b}{\bar{\nu}_d} E_d \quad (2.10)$$

$$\frac{dE_u}{dz} = \frac{a + b_b}{\bar{\nu}_u} E_u + \frac{b_b}{\bar{\nu}_d} E_d. \quad (2.11)$$

The two stream model offers computational utility in the uncoupling of the diffuse and upwelling streams. This uncoupling forms a system of two equations to be solved as two initial value problems instead of a boundary value problem. From here out the three stream model will be the basis set of equations to be solved for the optical model. The two stream will be referred to for its utility in special cases.

2.1 Solving Three Stream Equations

The three stream model is solved in the context of its application to the ROMS biogeochemical model. The downward direct stream, equation 2.1, can be solved independently from the set of coupled equations that describe E_d and E_s

(equations [2.2](#) and [2.3](#)), which are solved as a two dimensional, two point boundary value problem. Equations [2.1](#), [2.2](#), and [2.3](#) can be rewritten in vector form following [Dutkiewicz et al. \(2015\)](#),

$$\frac{dE_d}{dz} = C_d E_d \quad (2.12)$$

$$\frac{d\mathbf{E}}{dz} = \mathbf{M}\mathbf{E} + \mathbf{I}, \quad (2.13)$$

with boundary conditions designated by,

$$E_d(z=0) = E_{d0}, \quad E_s(z=0) = E_{s0}, \quad E_u(z=H) = 0 \quad (2.14)$$

where,

$$\mathbf{E} = \begin{bmatrix} E_s \\ E_u \end{bmatrix}, \quad \mathbf{M} = \begin{bmatrix} C_s & -B_u \\ B_s & -C_u \end{bmatrix}, \quad \mathbf{I} = \begin{bmatrix} -F_d \\ B_d \end{bmatrix} E_d, \quad (2.15)$$

and,

$$C_s = \frac{a + r_s b_b}{\bar{\nu}_s}, \quad B_u = \frac{r_u b_b}{\bar{\nu}_u}, \quad F_d = \frac{b_f}{\bar{\nu}_d}, \quad (2.16)$$

$$B_s = \frac{r_s b_b}{\bar{\nu}_s}, \quad C_u = \frac{a + r_u b_b}{\bar{\nu}_u}, \quad B_d = \frac{b_b}{\bar{\nu}_d} \quad (2.17)$$

2.1.1 Analytical Solution

In the case of constant absorption and scattering, either as the result of a pure seawater column or constant constituent profiles, an analytical solution can be derived. The solution for E_d is solved independently as an exponential decay of the downward direct light field,

$$E_d = E_{d0} e^{C_d z}. \quad (2.18)$$

The analytical solution for E_s and E_u is solved as the sum of the homogeneous and particular solution to equation [2.13](#) following [Dutkiewicz et al. \(2015\)](#). The solution

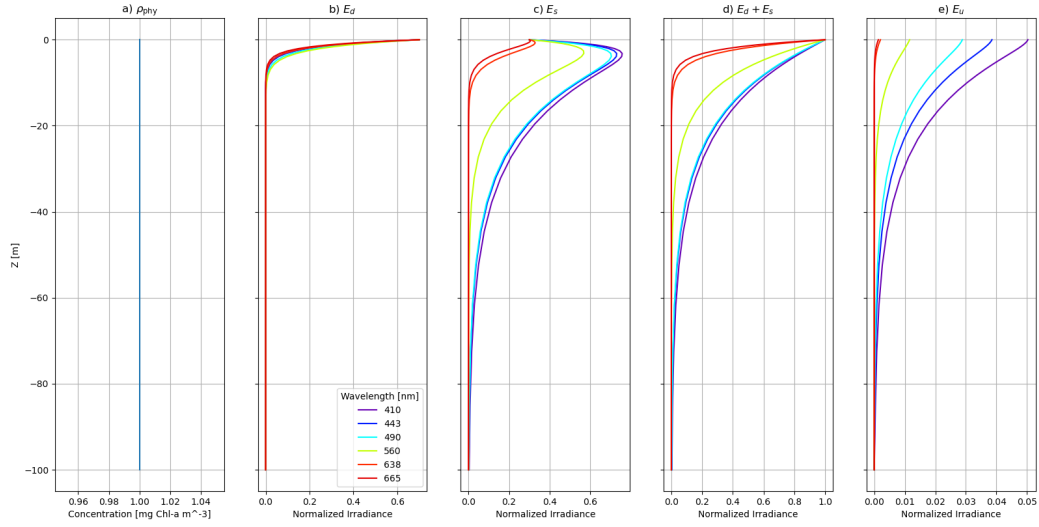


Figure 2.3: The analytical solution of the three stream model assuming a constant absorption and scattering for six different wavelengths. The irradiance streams shown are normalized such that $E_{s0} + E_{d0} = 1$ where for this case $E_{d0} = 0.7$ and $E_{s0} = 0.3$. a) Phytoplankton b) Downward direct irradiance. c) Downward diffuse irradiance d) Total downward irradiance (sum of downward direct and downward diffuse). e) Uppwelling irradiance stream. The irradiance streams are normalized such that $E_{d0} + E_{s0} = 1$ as explained in [2.3](#)

takes the following form,

$$\mathbf{E} = c_1 e^{\kappa_1 z} \mathbf{v}_1 + c_2 e^{\kappa_2 z} \mathbf{v}_2 + \begin{bmatrix} x \\ y \end{bmatrix} E_d \quad (2.19)$$

within eigenvalue, eigenvector pairs given by,

$$\kappa_1 = D - C_u, \quad \mathbf{v}_1 = \begin{bmatrix} 1 \\ \frac{B_s}{D} \end{bmatrix} \quad (2.20)$$

$$\kappa_2 = C_s - D, \quad \mathbf{v}_2 = \begin{bmatrix} \frac{B_u}{D} \\ 1 \end{bmatrix} \quad (2.21)$$

where,

$$D = \frac{1}{2} \left[C_s + C_u + \sqrt{(C_u + C_s)^2 - 4B_s B_u} \right], \quad (2.22)$$

and,

$$\begin{bmatrix} x \\ y \end{bmatrix} = \frac{1}{B_s B_u - (C_s - C_d)(C_u + C_d)} \begin{bmatrix} -(C_u + C_d) & B_u \\ -B_s & (C_s - C_d) \end{bmatrix} \begin{bmatrix} F_d \\ -B_d \end{bmatrix} \quad (2.23)$$

and constants of integration given by,

$$c_2 = \frac{E_{s0} e^{\kappa_1 H} \left(\frac{B_s}{D} \right) - x E_{d0} e^{\kappa_1 H} \left(\frac{B_s}{D} \right) + y E_d(z = H)}{\left(\frac{B_u B_s}{D^2} \right) e^{\kappa_1 H} - e^{\kappa_2 H}} \quad (2.24)$$

$$c_1 = E_{s0} - x E_{d0} - c_2 \frac{B_u}{D} \quad (2.25)$$

This analytical solution provides a means of solving the three stream irradiance field for constant absorption and scattering. This solution is demonstrated for a constant diatom phytoplankton profile in figure [2.3](#). The figure shows the three different irradiance streams as well as the sum of the two downward streams for six wavelengths. It is shown that the total downward irradiance ($E_d + E_s$) of longer (red) wavelengths attenuates more rapidly than that of the shorter (blue and green) wavelengths—this aligns with qualitative expectations of light dynamics in the ocean. In a true ocean modeling setting, the absorption and scattering will be non-constant, discrete, profiles, and therefore it is necessary to procure numerical solutions that are both accurate and stable.

2.1.2 Numerical Solutions

In the ocean, the absorption and scattering are variable profiles—functions of the concentrations of the different constituents—and thus equations [2.1](#), [2.2](#), [2.3](#) are solved via numerical methods. We formulate a constituent based vertical grid

and solve the three stream model using two different numerical methods, namely the shooting method and a semi-analytic inversion.

Numerical Grid Formulation

The vertical grid used for the computation of numerical solutions of the three stream model is constructed to a relative attenuation depth, H_A , that is either less than or equal to depth of the ocean floor, H . Due to the exponential decay of light in the water column, see [2.18](#) and figures [2.3](#), [2.4](#), the irradiance will often attenuate within a few tens to hundreds of meters (depending on the optical properties of the water). The bottom of the ocean's euphotic zone is taken to be the depth at which 1% of the surface light energy penetrates the water column ([Lorenzen, 1972](#)) and the euphotic zone for ocean environments from coastal opaque to oligotrophic clear waters varies from around 4.3 to 82.0 meters ([Lee et al., 2007](#)). On the other hand, the ocean floor in ROMS for the west coast domain reaches an upwards of 4,000 meters below the surface. In order to conserve computational resources it is only necessary to solve the light field to H_A instead of H . This choice also prevents numerical iterations for extended steps around near zero irradiance levels, which was found to support the numerical stability of the solution. The solution was unaffected by solving to H_A instead of H . In the case that H is less than H_A such as near shore portions of the regional domain, H was simply used instead.

H_A is wavelength-dependent and is taken to be the depth at which the total downward irradiance reaches 0.1 % of its surface value. That is $z = H_A$ such that,

$$\frac{E_d(z = H_A, \lambda) + E_s(z = H_A, \lambda)}{E_{d0} + E_{s0}} = 0.001. \quad (2.26)$$

This attenuation depth is found by numerically integrating equation [2.10](#) using the classical explicit fourth order Runge-Kutta (RK4) method. The grid is composed of a logarithmic spacing, mimicking the attenuating nature of the light fields. Thus the grids resolution is finest near the surface at high light field dynamics and then decays exponentially with depth. The log spacing and wavelength dependent H_A grid are demonstrated in figure [2.4](#). Finally, the grid is oriented to align with that of the ROMS vertical grid, with $z^{[k=0]} = H_A$ and $z^{[k=N-1]} = 0$.

Downward Direct

The downward direct stream, equation [2.10](#), is solved for independently as an initial value problem, with E_{d_0} as the initial value and using explicit RK4. The IVP is iterated from the surface downward to the bottom of the water column. The numerical solution to equation [2.13](#) is solved using two different methods described in the next sections.

Shooting Method

The first numerical method used to solve the coupled diffuse and upwelling streams (solving the two-point boundary value problem of equation [2.13](#)) is the shooting method. The shooting method formulates the boundary value problem (BVP) into a series of converging initial value problem (IVP) 'shots' by guessing the unknown boundary values at one boundary then iterating the IVP to the other boundary. For a given guess or iteration thereafter, the problem becomes a root finding problem in which the minimization of discrepancy between required boundary condition (BC) and solved boundary value (BV) at the final boundary is sought. This is achieved through iterative adjustments to the starting BV ([Press et al.](#),

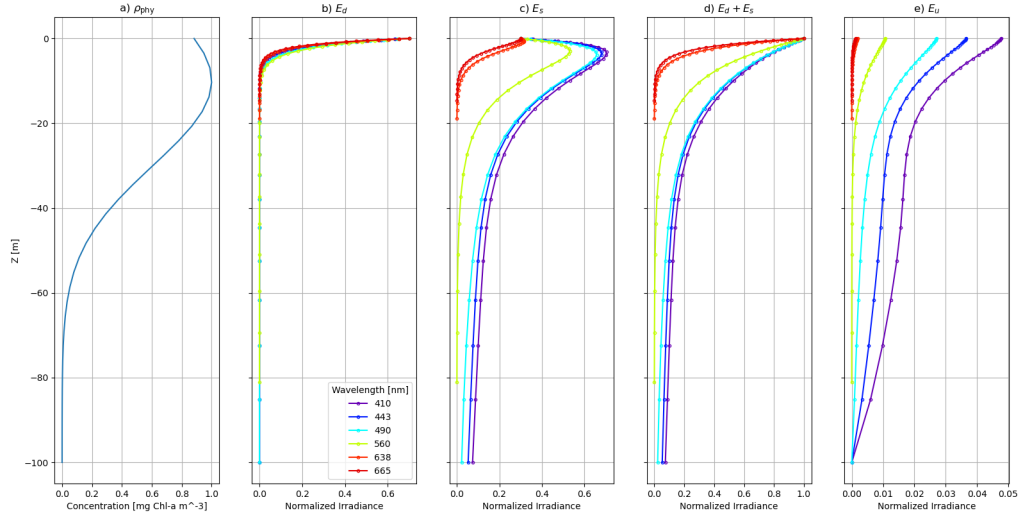


Figure 2.4: The three stream solution for an artificial phytoplankton profile with a sub-surface maximum in concentration. The solution assumes a single synechococcus phytoplankton type without the inclusion of CDOM or detritus. a) Artificial phytoplankton profile. b) Downward direct irradiance stream. c) Downward diffuse stream. d) Total downward irradiance, $E_d + E_s$. e) Upwelling irradiance stream. Six different wavelength solutions are provided with their line color correlating to their true optical color. The logarithmic grid spacing is shown by the points on each line, with the solution computed to a depth H_A which is shallower for longer wavelengths and deeper for shorter wavelengths.

(2007). We implement the secant method for our root finding approach, as described by Venturi (2022). Given the nature of the problem and the provided BCs there are two different directions in which shots can be taken to solve equation 2.13. Shots can be taken by iterating the IVP shots vertically upwards or downwards with each method described separately as follows.

The shooting down version works by guessing the unknown of $E_u(z = 0)$ and using the known BC of $E_s(z = 0) = \frac{E_{s0}}{17}$ to formulate equation 2.13 into an IVP

to be iterated from the surface down the water column. The bottom BC $E_u(z = H_A) = 0$ is then used as the metric for closeness of each shot's accuracy, which defines an error function between the resulting BV from the IVP solution and the required bottom BC (Venturi, 2022). The error function is given by,

$$J(E_u^{[j]}) = E_u(z = H_A, E_u^{[j]}(z = 0)) - 0 \quad (2.27)$$

$$= E_u(z = H_A, E_u^{[j]}(z = 0)), \quad (2.28)$$

where j represents the iteration, i.e., the current shot of the shooting method. The secant routine becomes,

$$E_u^{[j+1]}(z = 0) = E_u^{[j]}(z = 0) - \frac{E_u^{[j]}(z = 0) - E_u^{[j-1]}(z = 0)}{J(E_u^{[j]}) - J(E_u^{[j-1]})}, \quad (2.29)$$

which requires the two different initial guesses. By performing this shooting down iteratively, a solution is converged upon such that, $\lim_{j \rightarrow \infty} J(E_u^{[j]}) = 0$.

On the other hand, the shooting up version works by guessing the unknown boundary value of $E_s(z = H_A)$ and using the known BC $E_u(z = H_A) = 0$ to formulate equation 2.13 into an IVP to be iterated from the attenuation depth vertically upward to the surface. This approach gives an error function, using $E_s(z = 0) = E_{s0}$ as the metric of fit, as follows,

$$J(E_s^{[j]}) = E_s(z = 0, E_s^{[j]}(z = H_A)) - E_{s0}. \quad (2.30)$$

the secant method then becomes,

$$E_s^{[j+1]}(z = H_A) = E_s^{[j]}(z = H_A) - \frac{E_s^{[j]}(z = H_A) - E_s^{[j-1]}(z = H_A)}{J(E_s^{[j]}) - J(E_s^{[j-1]})}. \quad (2.31)$$

This sequence converges onto the solution in $\lim_{j \rightarrow \infty} J(E_s^{[j]}) = 0$.

For both shooting methods the classical explicit RK4 scheme is used for integrating the IVP in each shot. Furthermore, both shooting method versions are

guaranteed to converge in a finite number of shots—two initial guesses and one final solution iteration— because the system of equations [2.13](#) is linear at both boundaries ([Press et al., 2007](#)). This guarantee of convergence in a small number of shots proves to be an advantageous trait of the method.

Semi-analytic Inversion

The second numerical method implemented follows ([Dutkiewicz et al., 2015](#)), solving the analytical solution within each computational layer, k ,

$$\mathbf{E} = c_1^{[k]} e^{-\kappa_1^{[k]}(z-z^{[k]})} \mathbf{v}_1 + c_2^{[k]} e^{\kappa_2^{[k]}(z-z^{[k+1]})} \mathbf{v}_2 + \begin{bmatrix} x^{[k]} \\ y^{[k]} \end{bmatrix} E_d(z). \quad (2.32)$$

The eigenvectors are rewritten in the following form,

$$\mathbf{v}_1 = \begin{bmatrix} 1 \\ \frac{B_s}{D} \end{bmatrix} = \begin{bmatrix} 1 \\ r_1 \end{bmatrix} \quad (2.33)$$

$$\mathbf{v}_2 = \begin{bmatrix} \frac{B_u}{D} \\ 1 \end{bmatrix} = \begin{bmatrix} r_2 \\ 1 \end{bmatrix}. \quad (2.34)$$

The boundary conditions given by equations [2.14](#) become designated at compute layers $k = 0$ and $k = N - 1$ as follows,

$$c_1^{[0]} + r_2^{[0]} e^{-\kappa_2^{[0]} z^{[0]}} = E_{s0} - x^{[0]} E_{d0} \quad (2.35)$$

$$c_2^{[N-1]} = 0 \quad (2.36)$$

[Dutkiewicz et al. \(2015\)](#) enforces continuity at the computational boundaries in order to solve for the constants of integration within each layer,

$$e^{-\kappa_1^{[k]}(z^{[k+1]}-z^{[k]})} c_1^{[k]} + r_2^{[k]} c_2^{[k]} + x^{[k]} E_d(z^{[k+1]}) = \quad (2.37)$$

$$c_1^{[k+1]} + e^{\kappa_2^{[k+1]}(z^{[k+1]}-z^{[k+2]})} r_2^{[k+1]} c_2^{[k+1]} + x^{[k+1]} E_d(z^{[k+1]})$$

$$\begin{aligned}
& e^{-\kappa_1^{[k]}(z^{[k+1]}-z^{[k]})} r_1^{[k]} c_1^{[k]} + c_2^{[k]} + y^{[k]} E_d(z^{[k+1]}) = \\
& r_1^{[k+1]} c_1^{[k+1]} + e^{\kappa_2^{[k+1]}(z^{[k+1]}-z^{[k+2]})} c_2^{[k+1]} + x^{[k+1]} E_d(z^{[k+1]}).
\end{aligned} \tag{2.38}$$

Following [Dutkiewicz et al. \(2015\)](#), based on the work of [Kylling et al. \(1995\)](#) and [Toon et al. \(1989\)](#), the coupled equations [2.37](#) and [2.38](#) are reduced to a tridiagonal system as follows,

$$\begin{aligned}
& e^{-\kappa_1^{[k]}(z^{[k+1]}-z^{[k]})} (1 - r_1^{[k]} r_2^{[k+1]}) c_1^{[k]} + (r_2^{[k]} - r_2^{[k+1]}) c_2^{[k]} - (1 - r_1^{[k+1]} r_2^{[k+1]}) c_1^{[k+1]} = \\
& \left(x^{[k+1]} - x^{[k]} - (y^{[k+1]} - y^{[k]}) r_2^{[k+1]} \right) E_d(z^{[k+1]})
\end{aligned} \tag{2.39}$$

$$\begin{aligned}
& (1 - r_1^{[k]} r_2^{[k]}) c_2^{[k]} - (r_1^{[k+1]} - r_1^{[k]}) c_1^{[k+1]} - e^{-\kappa_2^{[k+1]}(z^{[k+2]}-z^{[k+1]})} (1 - r_2^{[k+1]} r_1^{[k]}) c_2^{[k+1]} = \\
& \left(y^{[k+1]} - y^{[k]} - (x^{[k+1]} - x^{[k]}) r_1^{[k]} \right) E_d(z^{[k+1]})
\end{aligned} \tag{2.40}$$

This tridiagonal system is then solved through an inversion of the matrix via an LU-decomposition algorithm. The solutions for $c_1^{[k]}$ and $c_2^{[k]}$ are then applied to the general solution in equation [2.32](#) which can then be solved to give E_s and E_u at any z . This semi-analytic inversion solution will hereafter be referred to as the Dutkiewicz solution.

Numerical Sensitivity

The sensitivity of each method—shooting down, shooting up, and Dutkiewicz—to grid resolution is shown in figure [2.5](#).a and [2.5](#).b. Each method is implemented for a constant diatom absorption and scattering profile of 1 mgChla m^{-3} . The error

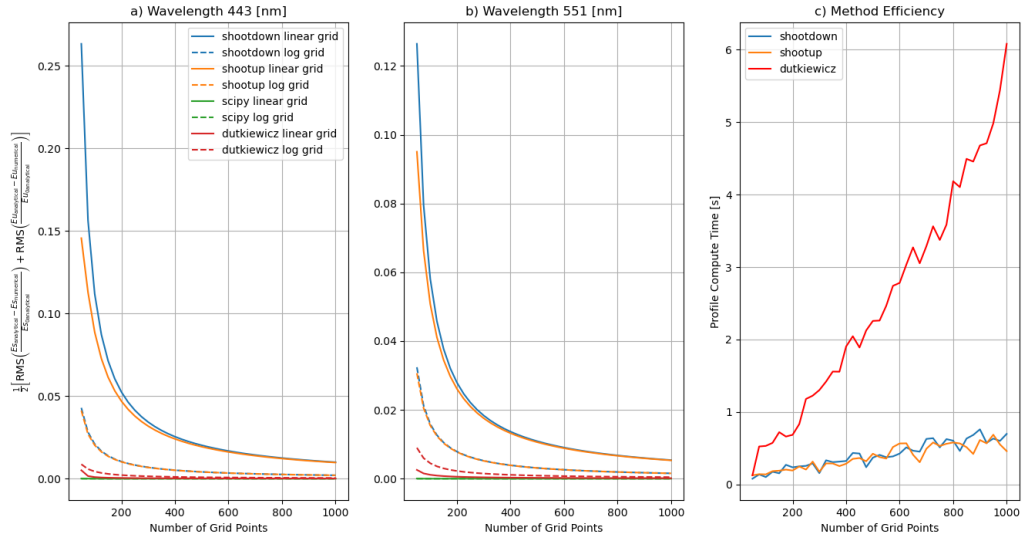


Figure 2.5: Sensitivity and efficiency of the different methods when compared to the analytical solution. a) Sensitivity to grid resolution for the wavelength of 443 nm. The y-axis is designated by the error function equation 2.41. b) Sensitivity to vertical grid resolution for the wavelength of 551 nm. c) The mean compute time per profile of the different methods.

of each method from the analytical solution is the taken as the mean of the RMS of the fractional bias across streams of each method such that,

$$E_{\text{err}} = \frac{1}{2} \left[\text{RMS} \left(\frac{E_{u_{\text{analytical}}} - E_{u_{\text{numerical}}}}{E_{u0_{\text{analytical}}}} \right) + \text{RMS} \left(\frac{E_{s_{\text{analytical}}} - E_{s_{\text{numerical}}}}{E_{s0_{\text{analytical}}}} \right) \right]. \quad (2.41)$$

The Dutkiewicz solution is more accurate than the shooting method for the same resolution grid (figures 2.5.a and 2.5.b); however, the improved accuracy comes with much greater computational cost that does not scale well with resolution as shown in figure 2.5.c. Using a logarithmic grid spacing greatly improves the accuracy of the two shooting method versions as shown by the dashed lines in figures 2.5.a and 2.5.b. The logarithmic grid actually worsens the accuracy of the Dutkiewicz

solution, most likely a repercussion of a poorer conditioned tridiagonal coefficient matrix.

While the Dutkiewicz solution provides an elegant and accurate means to solve the three stream model, the shooting up method is used as the default numerical solution in the optical model implementation into ROMS and further studies. This choice is due to the following advantages of the shooting method: the shooting method is fairly robust, easy to implement, computationally inexpensive, and does not involve an inversion. The shooting method also benefits from a predetermined number of iterations since the system is linear (Press et al., 2007). Through the implementation of a convergence test, the stability and accuracy of the method could be assured. The decision between shooting up and shooting down is motivated by the shooting up method performing better during stability tests at extremely low resolution. Finally, the shooting method is easily adaptable for improvements to accuracy and stability by using different IVP methods such as higher order or implicit schemes.

2.2 Estimating R_{rs} from Simulated Irradiance

The solution to the three irradiance streams must be translated into R_{rs} in order to be compared or assimilated with satellite ocean color data. R_{rs} is defined as the ratio of the water leaving radiance, $L_u(0^+, \theta, \phi, \lambda)$, to the downward irradiance, $E_d(0^+, \lambda)$, at a particular point just above the ocean surface (Mobley, 2021),

$$R_{rs}(0^+, \theta, \phi, \lambda) \equiv \frac{L_u(0^+, \theta, \phi, \lambda)}{E_d(0^+, \lambda) + E_s(0^+, \lambda)}, \quad (2.42)$$

where 0^+ designates the irradiance and radiance fields are just above the surface of the water. Two conversions are necessary to produce an R_{rs} from the three stream

solution output that is analogous to equation [2.42](#), the observed R_{rs} provided by satellite data. The first being the conversion of the upwelling irradiance, E_u , into upwelling radiance, L_u . The second conversion takes R_{rs} from just below the surface ($R_{rs}(0^-, \theta, \phi, \lambda)$) to R_{rs} just above the surface ($R_{rs}(0^+, \theta, \phi, \lambda)$). To convert E_u to L_u , a bidirectional function, Q , is used that defines the ratio between $E_u(0^-, \lambda)$ and $L_u(0^-, \theta, \phi, \lambda)$ ([Morel & Gentili, 1993](#)). $L_u(0^-, \theta, \phi, \lambda)$ is then written as,

$$L_u(0^-, \theta, \phi, \lambda) = \frac{E_u(0^-, \lambda)}{Q}. \quad (2.43)$$

The value of Q varies from 3 to 5 sr, but it has been shown by [Dutkiewicz et al. \(2018\)](#) and [Lee et al. \(2002\)](#) that the conversion to R_{rs} is insensitive to variation in the value of Q . We assume a median value of $Q = 4$ sr. Equation [2.42](#) can subsequently be rewritten in terms of the upwelling irradiance as follows,

$$R_{rs}(\lambda, 0^-) = \frac{1}{Q} \frac{E_u(0^-, \lambda)}{E_d(0^-, \lambda) + E_s(0^-, \lambda)} = \frac{1}{Q} \frac{E_{u0}(\lambda)}{E_{d0}(\lambda) + E_{s0}(\lambda)}, \quad (2.44)$$

The second conversion takes R_{rs} from just below the surface ($R_{rs}(0^-, \lambda)$) to R_{rs} just above the surface ($R_{rs}(0^+, \lambda)$). Following [Lee et al. \(2002\)](#) the transformation is given by,

$$R_{rs}(\lambda, 0^+) = \frac{0.52R_{rs}(\lambda, 0^-)}{(1 - 1.7R_{rs}(\lambda, 0^-))}. \quad (2.45)$$

This set of translations from E_u to L_u and $R_{rs}(0^-, \lambda)$ to $R_{rs}(0^+, \lambda)$ formulates the optically modeled irradiance into a R_{rs} comparable to that observed by satellite.

2.3 Normalized and Directional Surface Irradiance

The optical model of [Dutkiewicz et al. \(2015\)](#) relies upon the use of an atmospheric radiative transfer model, namely OASIM, in order to produce the surface

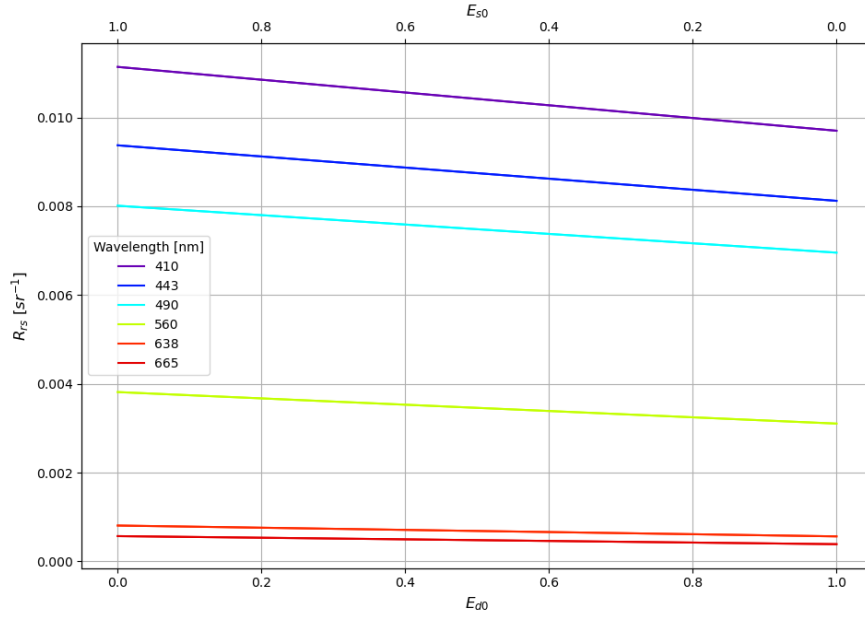


Figure 2.6: The sensitivity of R_{rs} to the directional choices for surface irradiance for different wavelengths. The top x-axis displays the value of surface diffuse E_{s0} and the bottom x-axis displays the value of the surface direct E_{d0} . The total downward irradiance at the surface remains constant with $E_{d0} + E_{s0} = 1$.

irradiance values for the diffuse and downward streams, E_{s0} and E_{d0} respectively. The implementation of surface irradiance values in our model relies on the nature of the calculation of the desired output, R_{rs} . As apparent in equation [2.44](#), R_{rs} is a function of the ratio of the upwelling irradiance at the surface to the sum of the two downward irradiance streams at the surface. The functional dependence on the dimensionless ratio, $\frac{E_{u0}}{E_{s0} + E_{d0}}$ allows us to represent the irradiance streams in terms of normalized irradiance such that each stream is divided by $E_{d0} + E_{s0}$. This approach allows for the setting of an arbitrary $E_{d0} + E_{s0} = 1$ without affecting the R_{rs} . However, this does not solve the directional problem with regard to the ratio of diffuse to downward direct irradiance. The ratio of diffuse to downward irradiance varies with a dependence on the state of the atmosphere including the time of day,

wavelength, levels of atmospheric gases, clouds, and aerosols (Gregg & Rousseaux, 2016).

While the directional component of the downward surface irradiance does vary, the solution for R_{rs} from the three stream model is fairly insensitive to large changes in the ratio of diffuse and direct downward irradiance. R_{rs} 's dependence, or rather independence, to the ratio of diffuse and direct is illustrated in figure 2.6. The R_{rs} is calculated as a function of different ratios of E_{d0} and E_{s0} for different wavelengths with constant $1 \text{ mg chl-a m}^{-3}$ diatom profiles. The shorter wavelengths show a higher dependence on E_{s0}/E_{d0} than longer wavelengths. Even so, the largest dependence is seen in wavelength 410nm, which between extremes of 100% E_{s0} and 100% E_{d0} returns less than a 22% change in R_{rs} . However, this small change could be important for the OCx algorithm, described in the next section, which uses a ratio of blue and green R_{rs} . Using this result E_{s0}/E_{d0} is set constant with $E_{d0} = 0.7$ and $E_{s0} = 0.3$ which mimics the conditions of a clear sky (Wald, 2018). It is shown in (Gregg & Casey (2009)) that the total surface irradiance $E_{d0} + E_{s0}$ changes significantly with wavelength, but for given atmospheric conditions $\frac{E_{s0}}{E_{d0}}$ is fairly independent between wavelengths 440-700. (Gregg & Casey (2009)) also shows the significant difference in $\frac{E_{s0}}{E_{d0}}$ as a result of atmospheric conditions, with majority diffuse on cloudy days and majority direct on clear days. For the purpose of satellite comparison, we assume cloud free atmospheric conditions since ocean color satellite observations are cloud free (Jouini et al. (2013)).

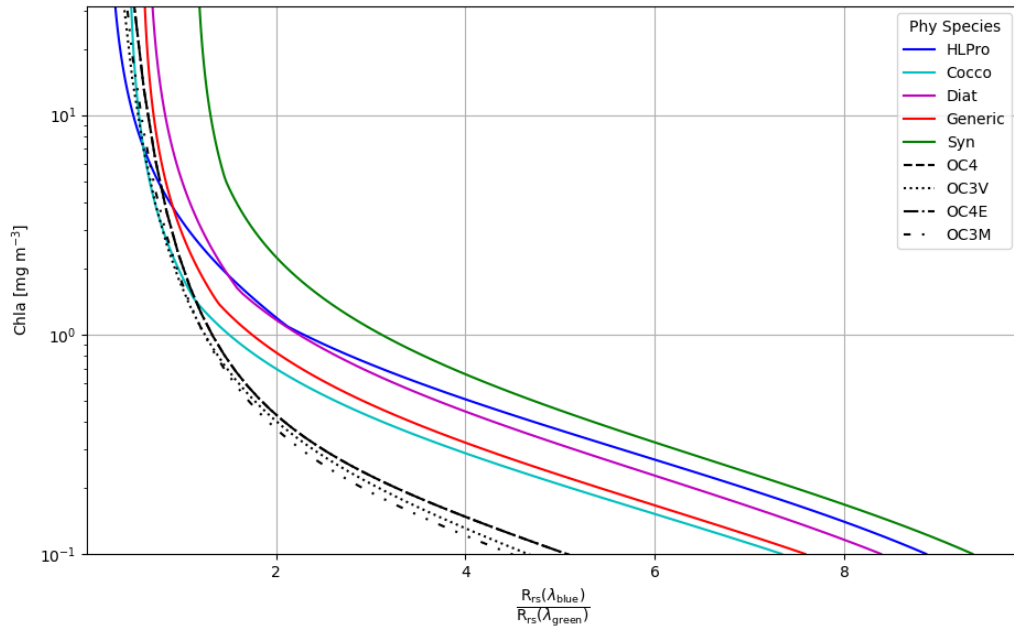


Figure 2.7: The relationship of chl-a and R_{rs} ratios for the optical model and for the NASA OCx algorithm. The differently styled black lines show chl-a as an output of the OCx algorithm for different ratios of R_{rs} . Each differently styled black line corresponds to a sensor-specific set of coefficients as provided by table 2.3. The colored lines show a ratio of R_{rs} as an output of the three stream model for different constant chl-a values. Each differently colored line corresponds to a specific phytoplankton type.

2.4 OCx Chlorophyll-a Ocean Color Algorithm

Satellite-observed chl-a is derived from observed R_{rs} using algorithms that rely on empirically derived coefficients from in situ and satellite R_{rs} observations such as that described by O'Reilly et al. (2000) and Werdell & Bailey (2005). Using such a tool to derive chl-a surface concentrations from modeled R_{rs} provides enables the comparison of optical model output to in situ chlorophyll-a. The ocean color algorithm used for this purpose is the NASA OCx algorithm, as described by O'Reilly

et al. (1998). The OCx algorithm is a function of R_{rs} values for green and blue wavelengths, where $R_{rs}(\lambda_{\text{green}})$ is sensor-specific and $R_{rs}(\lambda_{\text{blue}})$ is the largest R_{rs} value of two or three sensor-specific blue wavelengths as shown in table 2.3 taken from the NASA Ocean Color Website [1]. Sensor-specific refers to the fact that satellites observed ocean color (R_{rs}) differently and at different wavelengths. Each satellite has an intrinsic set of coefficients to account for these sensor based differences. The concentration of chl-a is calculated in the OCx algorithm as a “fourth-order polynomial relationship” as follows,

$$\log_{10}(c_a) = a_0 + \sum_{i=1}^4 a_i \left(\log_{10} \left(\frac{R_{rs}(\text{blue})}{R_{rs}(\text{green})} \right) \right)^i, \quad (2.46)$$

where c_a is the concentration of chl-a per cubic meter¹. The coefficients a_0 , a_1 , a_2 , a_3 , and a_4 are also sensor-specific as shown in table 2.3. This conversion from R_{rs} to chl-a allows for the direct comparison of R_{rs} values calculated from the light model to in situ chlorophyll-a values. It also allows for the comparison of satellite-derived chlorophyll-a estimates to optical model estimates.

Method	blue [nm]	green [nm]	a ₀	a ₁	a ₂	a ₃	a ₄
OC4	$R_{rs}(443, 490, 510)$	$R_{rs}(555)$	0.33	-2.99	2.72	-1.22	-0.57
OC3V	$R_{rs}(443, 486)$	$R_{rs}(550)$	0.22	-2.47	1.59	-0.43	-0.78
OC4E	$R_{rs}(443, 490, 510)$	$R_{rs}(560)$	0.33	-2.77	2.44	-1.13	-0.50
OC3M	$R_{rs}(443, 488)$	$R_{rs}(547)$	0.24	- 2.74	1.80	0.00	-1.23

Table 2.3: The sensor specific OCx ocean color algorithm coefficients. Coefficients are provided by the NASA Ocean Color Website¹.

Using the OCx algorithm the relationship between $\frac{R_{rs}(\text{blue})}{R_{rs}(\text{green})}$ and Chla is

¹NASA Ocean Color Website https://oceancolor.gsfc.nasa.gov/atbd/chlor_a/

demonstrated for different sensors in figure [2.7](#). Also on that same figure the inverse dependence, R_{rs} ratio as a function of constant chlorophyll-a profiles, as computed by the optical model for different phytoplankton types is plotted. For values less than 1 mg Chl-a m^{-1} the OCx and three stream model do not correlate well; however values above 1 mg Chl-a m^{-1} OCx and the model do correlate well.

An exact correlation is not expected since the OCx method is derived from ocean observed data and represents surface chl-a values, not subsurface. In the ocean chl-a profiles are generally not constant, exhibiting concentrations that decrease away from the surface or have subsurface maxima. The structure of the profile has been shown to influence R_{rs} ([Stramska & Stramski, 2005](#)). Thus figure [2.7](#) should be examined under pretense that the profiles input to the three stream model are constant with depth and that is analogous but does not necessarily correlate with the surface valued chl-a concentrations computed by the OCx algorithm. Also, natural water samples have a phytoplankton community, detritus, CDOM, and other unresolved constituents, which are not represented in the single phytoplankton results shown here, but inevitably influence empirical results. This systemic difference exists between the chl-a input to the model and the chl-a it produces using the OCx algorithm. For our calculation of chl-a from modeled R_{rs} we follow [Jones et al. \(2016\)](#) and implement the OC3M coefficients.

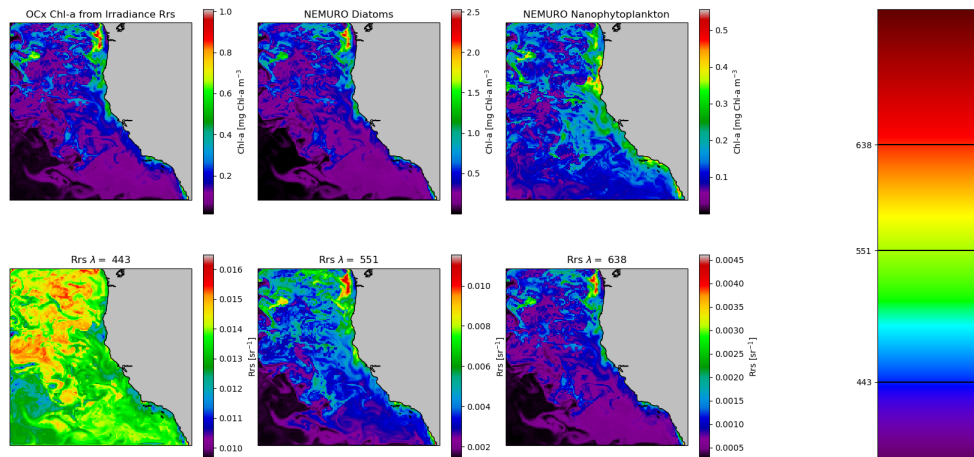


Figure 3.1: The results of applying the optical model to a single time step of the biogeochemical model. The top row (From left to right) shows the OCx chl-a derived from optical model R_{rs} , the chl-a of the biogeochemical model large phytoplankton class, the chl-a of the biogeochemical small phytoplankton class. The bottom row shows the optical model R_{rs} for wavelengths (left to right) 443 nm, 551 nm, 638 nm.

3

Validation of the Optical Model

The optical model is coupled to a regional model of the CCS which spans the west coast of the United States. The regional model constructed with ROMS

simulates the coupled physical and biogeochemical dynamics of the west coast domain, including two groups of phytoplankton species, namely, nanophytoplankton (assumed to be *synechococcus*) and diatoms. The surface concentrations of diatoms and nanophytoplankton are shown in [3.1](#). From the output of the three dimensional biogeochemical model, one can use the optical model to calculate irradiance profiles and formulate R_{rs} . The optical model R_{rs} output is shown in figure [3.1](#). This includes R_{rs} for three different wavelengths and OCx calculated surface chl-a.

While the optical model could be implemented for the assimilation of R_{rs} to correct fields, it would be difficult to ascertain whether discrepancies result from the inaccurate outputs of the biogeochemical model or inaccuracies with the optical model implementation. Thus, it is necessary to test the stand-alone optical model by using observations as input and comparing output to either in situ or satellite observations. A correlation of optical model output to observations would provide validation of the model and would ensure confidence in the use of the optical model to formulate accurate estimations of R_{rs} from biogeochemical model variables in data assimilation.

Section [3.1](#) uses in situ cruise and satellite observations to validate the implementation of all three stages (absorption and scattering estimations, irradiance solutions, and translation to R_{rs} and chl-a) of the optical model together. Section [3.2](#) uses anchored profiler data to validate the first two stages of the optical model separately. Together, these validation efforts provide a comprehensive study on the implementation of the ocean optics model and its utility for future assimilation purposes.

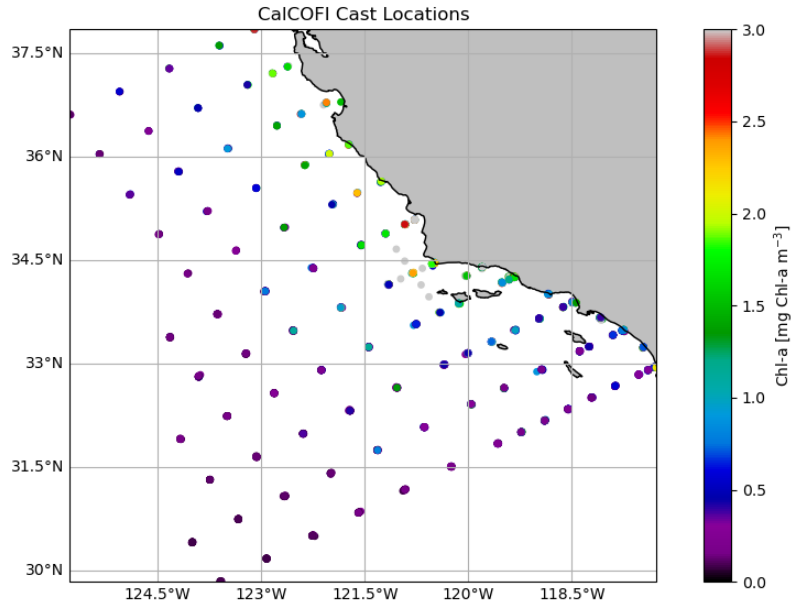


Figure 3.2: The locations of different CalCOFI cruise casts as well as their accompanying surface chlorophyll-a concentrations. Many of the casts overlap each other with similar cast positions being used in over the temporal extent of the data set.

3.1 CalCOFI and CCI Validation

To validate the optical model requires two separate data observations: in situ observations of water constituents (to calculate absorption and scattering profiles) and satellite ocean color observations (for comparison of model output). This work aims to validate all stages of the optical model, including the estimation of absorption and scattering from constituents, solving the three stream irradiance equations, and the translation of irradiance fields to R_{rs} and chl-a.

3.1.1 Data Acquisition

For constituent profiles, chl-a profile data is obtained from a series of California Cooperative Oceanic Fisheries Investigations (CalCOFI) cruises¹. The profiles correspond to individual casts taken at locations in a portion of the west coast domain as shown in figure 3.2. Satellite observations (R_{rs} and chl-a) are obtained from the Ocean Colour Climate Change Initiative (CCI) project database². CCI provides a data set of daily ocean color observations composed of different sensors including VIIRS, MODIS, MERIS, OLCI, and SeaWiFS. For each CalCOFI cast a nearest neighbor (in both space and time) CCI observation was found. Since the temporal resolution of the CCI data is 24 hours, the CCI and CalCOFI nearest neighbor match is bounded by 12 hours in time. Furthermore, the spatial match is restricted such that the nearest CCI observation is within a 2 km radius of the CalCOFI cast location. We consider all CalCOFI cast data from years 2012-2019 and are able to match 29% of casts with a CCI satellite observation for a total of 628 validation data points.

3.1.2 Implementing the Optical Model

The optical model is solved under the assumption that the chl-a in situ profile is composed of a single phytoplankton type such that,

$$a_{\text{phy}} = \alpha_{\text{phy}_i}(\lambda)\rho_{\text{phy}_i}(z) \quad (3.1)$$

$$b_{\text{phy}} = \beta_{\text{phy}_i}(\lambda)\rho_{\text{phy}_i}(z). \quad (3.2)$$

¹<https://calcofi.org/>

²<https://www.oceancolour.org/>

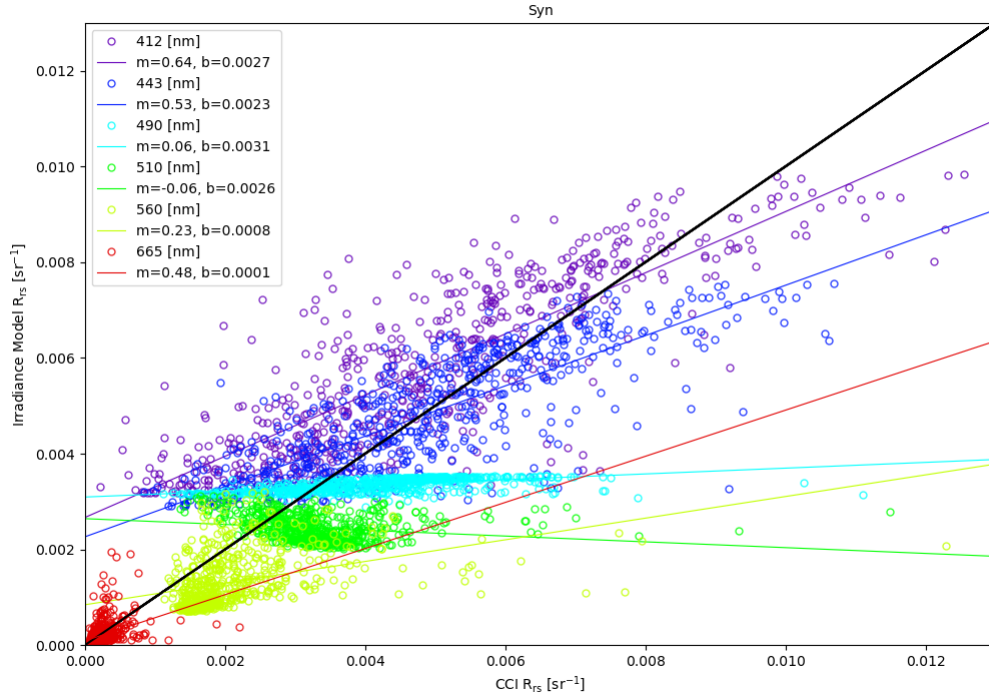


Figure 3.3: The CCI R_{rs} , x-axis, compared to optically modeled synechococcus R_{rs} , y-axis, for different wavelengths. The best fit lines for each R_{rs} wavelength comparison are plotted as well, the slopes, m , and intercepts, b , are designated in the legend of the figure. Wavelength marker colors correspond to their true optical color.

This results in a set of irradiance field solutions that are converted to wavelength and phytoplankton type dependent R_{rs} at each CalCOFI cast location. The CCI data contains R_{rs} at wavebands of 412 nm, 443 nm, 490 nm, 510 nm, 560 nm, and 665 nm. The optical model is run for all CCI wavelengths. Finally, modeled R_{rs} is translated into chl-a using the OCx algorithm, equation 2.46. The model is run for all 628 CalCOFI profile and CCI validation points.

3.1.3 R_{rs} Correlation

The correlation between modeled R_{rs} using CalCOFI chl-a profile input and CCI satellite measured R_{rs} is shown for synechococcus in figure 3.3. While the correlation is imperfect for some wavelengths and better for others, there are some important takeaways. First, the R_{rs} behaves as expected over different wavelengths, with shorter wavelengths producing higher R_{rs} and longer wavelengths producing smaller R_{rs} ; this was also shown in Dutkiewicz et al. (2015) on a global scale. For the majority of the wavelengths the slope of the best fit line is positive indicating the correct relationship with increasing CCI R_{rs} . This wavelength based correlation structure is quite different for each of the eight modeled phytoplankton types.

To illustrate the correlation across all phytoplankton types, the relative mean bias (RMB) and the root mean square relative error (RMSRE) between modeled and observed R_{rs} are shown for each CCI wavelength and each phytoplankton type in figure 3.4. Even though correlation overall is imperfect, different phytoplankton types exhibit different R_{rs} results—some types correlate better to CCI observations than others—illustrating the sensitivity of the solution to constituent variation. It is worth noting the inclusion of CDOM improves mean RMSRE across all phytoplankton types and wavelengths by 10% , showing that the solution is sensitive to variation in constituents other than different phytoplankton types. Synechococcus, low light prochlorococcus, high light prochlorococcus, and large eukaryotes display relatively small RMSRE across wavelengths compared to the correlations of diatoms and trichodesmium. Also, R_{rs} RMB is in different directions for different species (some species underestimate R_{rs} and others overestimate it).

These results suggest that there exists an optimal $a(\lambda)$ and $b(\lambda)$ that would

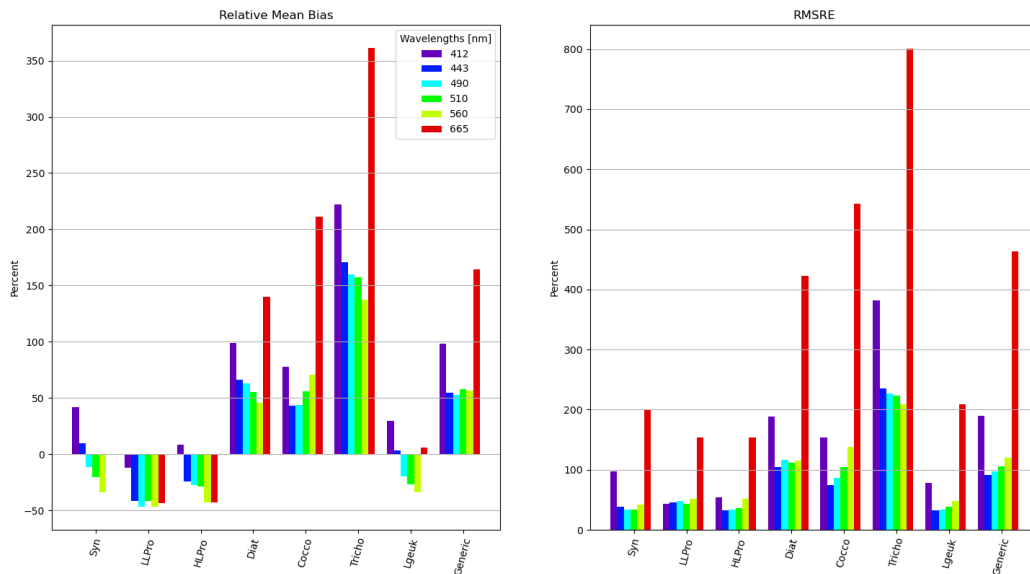


Figure 3.4: Left) The relative mean bias of the R_{rs} correlation as a percentage for all CCI wavelengths for each phytoplankton type. Right) The RMSRE of the R_{rs} correlation for all CCI wavelengths for each phytoplankton type.

minimize the difference between modeled and observed R_{rs} across wavelengths. Based on the directional bias of the different phytoplankton types, that optimal absorption and scattering structure could be formulated as a composite of the absorption and scattering of different phytoplankton types. Thus, the species-dependent RMSRE and directional RMB imply that single phytoplankton type chl-a profiles are a crude assumption. Likely profiles are composed of a community structure consisting of multiple phytoplankton types at different respective chl-a concentrations (as is found in nature). This is equivalent to using equations [2.6](#) and [2.7](#) instead of [3.1](#) and [3.2](#) respectively. Furthermore, true community structure is a function of space and time, making it such that each CalCOFI cast is composed of different communities representing distinct observed R_{rs} values.

The high sensitivity of R_{rs} to phytoplankton type and the realization of

the potential existence of an optimal dynamic community structure is the very reason for using R_{rs} for biogeochemical assimilation. The main challenge here is that the true community structure is unknown. The cast data does not include observations of the relative concentrations of different phytoplankton types—hence the single type chl-a assumption in the first place. This means there is no way to directly model the impact that accurate community estimation would have on these results. It is unknown if accurate community estimates would produce accurate R_{rs} values. Even without community observations, the results are important. The main takeaway is that modeled R_{rs} reflects variation in optical constituents which demonstrates the model’s utility in biogeochemical model assimilation. However, without explicit observation of constituent composition and community structure it is unknown if modeled R_{rs} accurately reflects constituent dynamics. In other words, without accurate representation of the first stage of the optical model (absorption and scattering estimation) it is not clear that modeled R_{rs} is accurate. Still, the results demonstrate alignment with observations for certain phytoplankton types.

3.1.4 Chlorophyll-a Correlation

Next, chl-a optical model output is compared to in situ CalCOFI chl-a and CCI satellite derived chl-a. In order to confidently compare modeled chl-a values to observations, the implementation of the OCx algorithm is first validated. CCI provides its own remote sensing derived chl-a product as part of the R_{rs} data set. The OCx implementation is validated by computing chl-a from CCI R_{rs} using the OCx algorithm and comparing those values to the CCI provided chl-a product. The comparison is shown in figure 3.5 where it is clear that the two different chl-a formulations correlate well. There is slight disagreement, mainly with the OCx algorithm

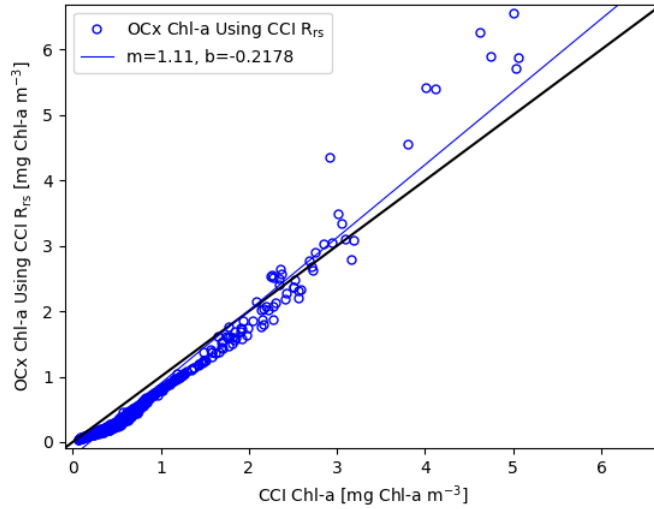


Figure 3.5: Chl-a derived from CCI R_{rs} using the OCx algorithm (y-axis) compared to CCI formulated, satellite chl-a (x-axis).

underestimating CCI chl-a. Slight discrepancies are to be expected since an empirical derivation of the relationship between R_{rs} and chl-a will vary between the OCx and CCI method. Overall the methods align, and as a result the implementation of the OCx algorithm can be used confidently.

The correlation between optically modeled chl-a and in-situ CalCOFI chl-a is the first to be examined. The correlation for the different phytoplankton types is shown in figure 3.6. The figure also shows the relative density of the number of observations for different chl-a bins. It is apparent that each phytoplankton type produces optically modeled chl-a with a distinct relationship to in situ chl-a. This comparison also demonstrates that the optical model retrieves similar chl-a values as were input for certain phytoplankton types. The sensitivity of the correlation to phytoplankton type further enforces the hypothesis that community estimation plays a significant role in optical model output. The density plot in 3.6 illustrates that the majority of in situ observations are less than 1 mgchl-a m⁻³. The effect of

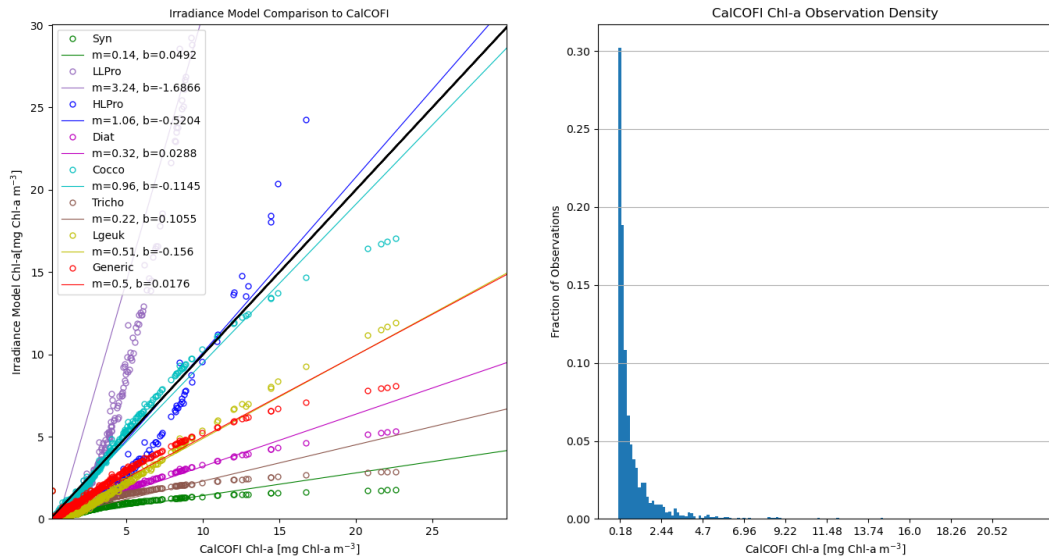


Figure 3.6: Left) The irradiance optically modeled chlorophyll-a, y-axis, compared to the in situ CalCOFI chlorophyll-a, x-axis, for different phytoplankton types. The legend provides the best fit line with slope m and intercept b . Right) A histogram showing the percentage of total in situ CalCOFI observations in different chlorophyll-a bins.

this density is shown in figure 3.7.a, where for all phytoplankton types, the optical model underestimates chl-a, showing a difference from what is qualitatively observed in figure 3.6.

The optical model's underestimation of in situ chl-a is a significant result that hints at systemic error in the formulation of chl-a from R_{rs} . This underestimation strongly correlates with the deviations between OCx and the optical model shown figure 2.7, specifically for low chl-a values. In figure 2.7, for a given constant chl-a input, the model returns a R_{rs} ratio which the OCx algorithm interprets to be lower than the initial input chl-a value. This is especially true for chl-a values less than 1 mgChla m⁻³. The majority of CalCOFI values are also less than 1 mgChla

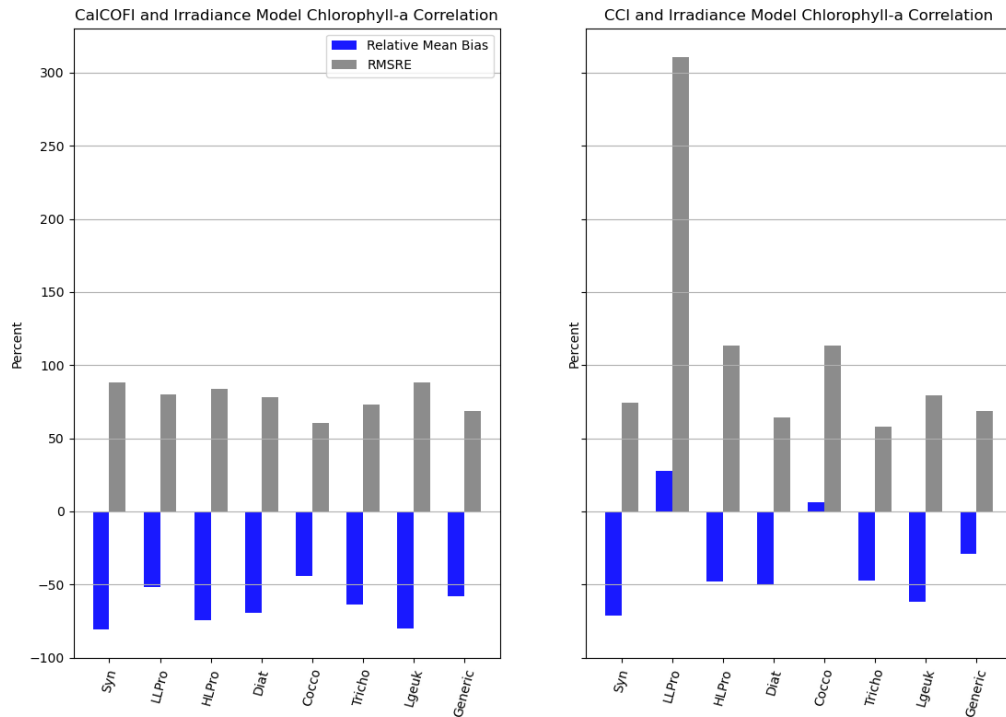


Figure 3.7: Left) The correlation statistics for the comparison of modeled chlorophyll-a to in situ CalCOFI observations. The blue bars represent the RMB and the grey bars measure the RMSRE. Each phytoplankton type is designated on the x-axis and has a corresponding set of RMB and RMSRE values. Right) The same plot as left but for the correlation of the optical model and the CCI chlorophyll-a m^{-3} and therefore this systemic underestimation of chl-a by all types is likely the result of an inherent relationship between the chl-a optical input, the R_{rs} ratio, and the OCx algorithm. It has been shown that methods other than the OCx algorithm provide improved estimates for low chl-a levels (e.g., [Hu et al. \(2012\)](#)). Future implementation of a method like this could improve correlations at low concentrations.

Optically modeled chl-a is also compared to CCI satellite derived chl-a as shown in figure [3.8](#). All observations are less than $5 \text{ mg Chl-a m}^{-3}$ with the majority being between $0\text{-}1 \text{ mg Chl-a m}^{-3}$ as shown in the accompanying density plot. It was

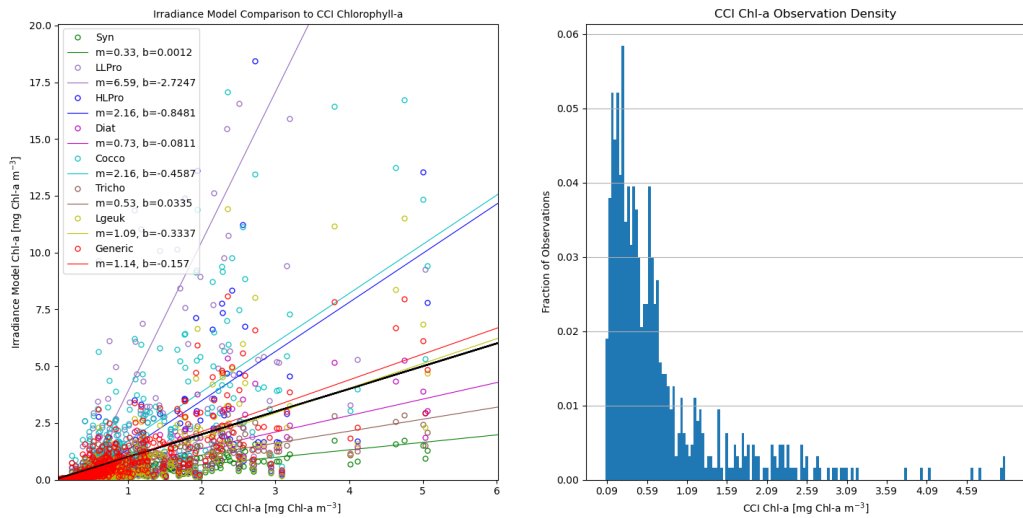


Figure 3.8: Left) The optically modeled chlorophyll-a compared to the CCI satellite derived chlorophyll-a product for different phytoplankton types. Right) The observation density histogram displaying the fraction of CCI observations for different chlorophyll-a bins.

previously shown that the OCx algorithm does a good job estimating CCI derived chl-a from CCI R_{rs} . Therefore, the disagreement in modeled and CCI chl-a directly results from the demonstrated discrepancies in R_{rs} . Figure 3.7 shows that modeled chl-a correlates to in situ better than satellite derived chl-a.

The final relationship analyzed is the correlation of CCI chl-a and in situ CalCOFI chl-a. This relationship is shown in figure 3.9 and shows disagreement with a RMSRE of 49%, RMB of -7.2%, slope of 0.25, and an r^2 of 0.54. This discrepancy is an important result, as in essence this is the correlation we are aiming to achieve through our attempts to model R_{rs} . This relationship represents the correlation of in situ to satellite data that would be implemented in the current chl-a based assimilation method. This poor correlation implies potential imperfections in the match between in situ and satellite data. There are many factors that could

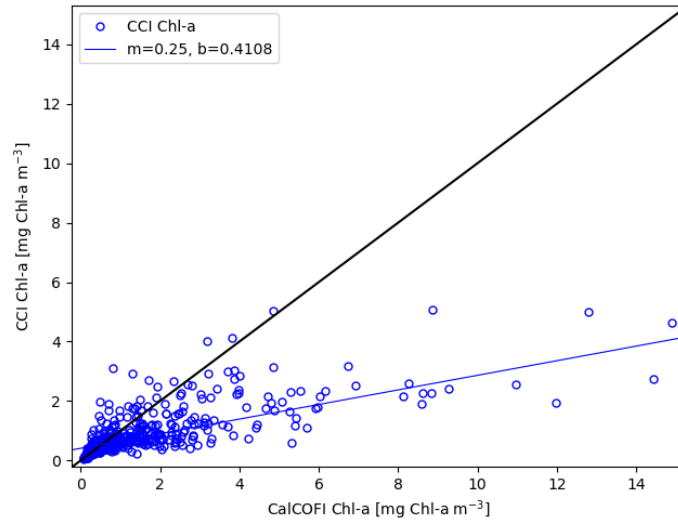


Figure 3.9: The CCI Chl-a product, y-axis, compared to surface CalCOFI in situ chl-a. The best fit slope and intercept are 0.25 and 0.4108 respectively.

contribute to the observed differences. One potential issue is that the designated satellite grid node to cast position match, even at less than the designated 2 km distance, is too large. Another possibility is the inaccurate formulation of *surface* chl-a with regards to what actually defines the surface of the in situ observations.

The mean surface depth across the 628 CalCOFI casts used is -0.033 meters, however empirically derived coefficients could result from a variable surface depth that does not correlate exactly to the surface level used here. Inherent differences in the comparison of satellite to in situ data has continually been a challenge for ocean modeling community due to distinct differences between the two observation methods. There is a tremendous amount of effort involved in formulating global in situ and satellite validation data sets, see [Werdell & Bailey \(2005\)](#). Therefore the observed discrepancies in our highly regional and self formulated optical validation data are not a surprising result. There are many things that could influence the potential match-up of satellite and in situ cruise data, regardless of the exact reason,

the fact that discrepancy exists favors the observed optical model R_{rs} results.

3.1.5 Summary

The main takeaways from the results presented thus far are as follows. The optical model R_{rs} and chl-a are highly sensitive to spectrally resolved absorption and scattering input profiles. The absorption and scattering profiles, and therefore the model itself, depend on the assumed phytoplankton type, with some types showing better correlation to observations than others. The high sensitivity of R_{rs} to phytoplankton type is an expected by-product of a tool that is to be utilized for biogeochemical assimilation. Modeled R_{rs} discrepancies are also wavelength dependent, with improved correlation for smaller wavelengths. Also, different community types exhibit different directional bias, suggesting that phytoplankton community structure with the potential for 4-D evolution, as is found in nature, would be of importance in accurately resolving absorption profiles. The model tends to underestimate in situ values of chl-a at low surface concentrations levels. This mimics the systemic bias shown between the OCx algorithm and model as shown in figure [2.7](#).

Finally, the differences between satellite and in situ observations of chl-a provide reason to believe that the model performs better than deduced originally. The differences illustrate the inherent inaccuracies in comparing in situ to satellite data. In other words, the optical model results are reasonable, in spite of in situ disagreement with satellite chl-a.

Using what was learned from comparing the model using in situ input to satellite observation, specifically motivated by inherent discrepancies between satellite and in situ data, the remainder of the model validation work is formulated using fully direct in situ input and output comparisons.

3.2 OOI Surface Piercing Profiler Validation

For further analysis of the optical model performance, a fully in situ validation approach is taken. The analysis seeks to validate the first and second stages of the optical model, absorption and scattering estimates and solving the irradiance streams respectively.

3.2.1 Data Acquisition

For this validation the extensive set of ocean optics data provided by the National Science Foundation's Ocean Observatories Initiative (OOI) Oregon Shelf Surface Piercing Profiler Mooring (CE02SHSP³). As the long name suggests, this OOI profiler is located on the Continental Shelf just off the Oregon coast, specifically at 44.6372°N, 124.299° W, and is anchored at a depth of 81m. The profiler uses various instruments to measure significant biogeochemical quantities, including optically important instruments such as a 3-wavelength fluorometer (FLORT), Spectrophotometer (OPTAA), and Spectral Irradiance (SPKIR). The combination of these three instruments provides profiles of fluorometric chl-a, beam attenuation, absorption, and downward spectral irradiance (as well as numerous other measurements). These OOI profiler observations are performed in sets of time series based deployments, with each deployment lasting around 2 months. In the work that follows we focus on the use of deployment 15, which extends from August 13th, 2019 to October 14th, 2019 with a total of 49 profiles. The first validation performed is comparison of modeled absorption and scattering to OOI OPTAA observed fields over wavelengths. This shows comparisons between modeled and observed spectral

³<https://oceanobservatories.org/site/ce02shsp/>

absorption and scattering as well possible corrections to discrepancies. For the second validation effort we compare the irradiance fields themselves, namely the total modeled downward irradiance $E_d + E_s$ to that measured by the OOI SPKIR.

3.2.2 Absorption and Scattering

The first stage of the optical model is the estimation of $a(\lambda)$ and $b(\lambda)$ from constituents and their parametrizations. Proper estimation sets the foundation for an accurate simulation of light dynamics, so comparisons between modeled and observed $a(\lambda)$ and $b(\lambda)$ serve as the starting point for our OOI validation work. The OOI OPTAA provides a measure of $a(\lambda)$ and total beam attenuation, $c(\lambda)$, where $c(\lambda)$ represents the sum of $a(\lambda)$ and $b(\lambda)$. Thus scattering is simply $c(\lambda) - a(\lambda)$. The OOI absorption (a_{OOI}) and scattering (b_{OOI}) are observed at 85 wavelengths between 400.3 nm and 735.8 nm. a_{OOI} and b_{OOI} are also processed to remove the effects of water. In effort to compare directly to the phytoplankton based coefficients of absorption and scattering—recall α and β (units of $\text{m}^2\text{mgchl}^{-1}$)—we compute the following,

$$\alpha_{\text{OOI}} = \frac{a_{\text{OOI}} - a_{\text{CDOM}}(\lambda, \text{Chl}_{\text{OOI}})}{\text{Chl}_{\text{OOI}}} \quad (3.3)$$

$$\beta_{\text{OOI}} = \frac{b_{\text{OOI}}}{\text{Chl}_{\text{OOI}}}. \quad (3.4)$$

The comparison of α_{phy} , β_{phy} and α_{OOI} , β_{OOI} is provided in figure [3.10](#). The figure shows the mean of α_{OOI} and β_{OOI} over all 49 profiles ($\bar{\alpha}_{\text{OOI}}$ and $\bar{\beta}_{\text{OOI}}$), as well as the region between its 20%-80% quantiles and the region between is extrema. α_{phy} and β_{phy} are shown on the same figure for different types.

Figure [3.10](#) shows that the β_{phy} agrees well with $\bar{\beta}_{\text{OOI}}$ and is on order of magnitude for most types. Absorption on the other hand shows significant disagree-

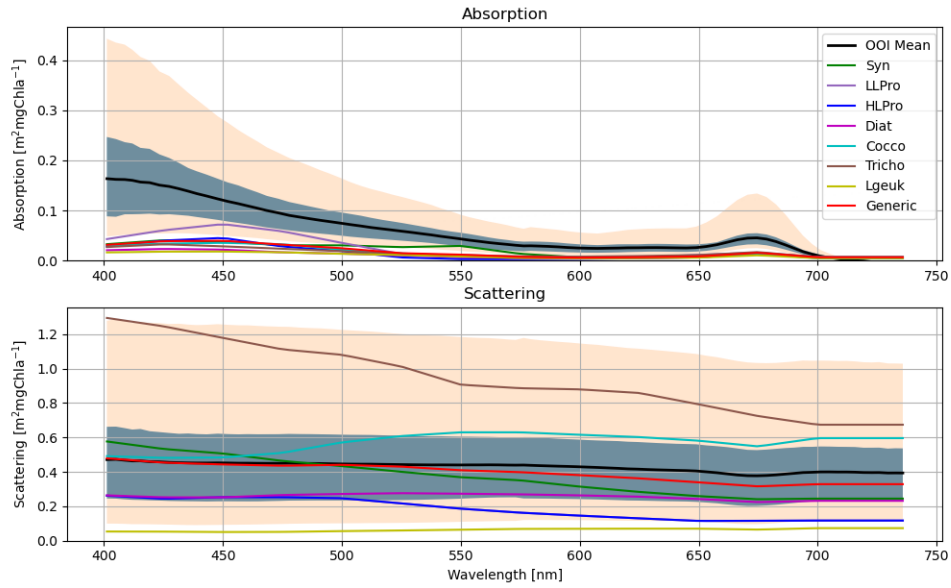


Figure 3.10: Top) The black line shows the mean OOI absorption as a function of wavelength for deployment 15. The grey shading shows the OOI absorption extent between the 20% and 80 % quantiles. The tan shading shows the maximum and minimum extent of OOI absorption. The colored lines correspond to the modeled absorption for different single species approximations. Bottom) Same as top, but for scattering instead of absorption.

ment. In particular, α_{phy} underestimates $\bar{\alpha}_{\text{OOI}}$ by about 2-4 orders of magnitude. This underestimation reflects the difficulty in resolving all optically significant constituents. The fact that $\bar{\alpha}_{\text{OOI}}$ is underestimated while $\bar{\beta}_{\text{OOI}}$ compares well specifically hints that CDOM is not being properly resolved. CDOM only effects total absorption and not scattering as shown in Dutkiewicz et al. (2015). Disagreement between α_{phy} and $\bar{\alpha}_{\text{OOI}}$ is largest at short wavelengths. This discrepancy at short wavelengths further supports an underestimation of CDOM since CDOM absorption is largest at short wavelengths and decays with increasing wavelength as shown in Kitidis et al. (2013). Finally, the OOI CE02SHSP site is just under 20km West from

the mouth of the Yaquina Bay which could provide a terrestrial source of CDOM, making for levels higher than approximated by equation 2.9.

To test this CDOM underestimation hypothesis we attempt a different CDOM approximation by using a CDOM-specific absorption following Dutkiewicz et al. (2015). This method gives absorption due to CDOM as,

$$a_{\text{CDOM}}(\lambda) = a_{\text{CDOM}_0}(\lambda_0)e^{-S_{\text{CDOM}}(\lambda-\lambda_0)}, \quad (3.5)$$

where $a_{\text{CDOM}_0}(\lambda_0)$ is the CDOM specific absorption at reference wavelength λ_0 . The spectral slope, following Dutkiewicz et al. (2015), is taken from Kitidis et al. (2013) and is $S_{\text{CDOM}} = 0.021 \text{ nm}^{-1}$. We take $a_{\text{CDOM}_0}(\lambda_0)$ to be,

$$a_{\text{CDOM}_0}(\lambda_0) = f_a[a_{\text{total}}(\lambda_0) - a_{\text{wat}}(\lambda_0)] = f_a a_{\text{OOI}}(\lambda_0), \quad (3.6)$$

where f_a represents the fraction of water free absorption that is composed of CDOM. Dutkiewicz et al. (2015) estimates the evolution of CDOM absorption using a ‘‘CDOM-like tracer’’ and a constant $a_{\text{CDOM}_0}(\lambda_0)$.

Using equation 3.5 with $f_a = 0.85$ and $\lambda_0 = 400$ the $\bar{\alpha}_{\text{OOI}}$ is recalculated and the resulting comparison is shown in figure 3.11. The differences between $\bar{\alpha}_{\text{OOI}}$ and α_{phy} are significantly lessened using this approach.

This method works because of access to $a_{(\text{OOI})}$, without such explicit observations, as in the biogeochemical model, this method can not be used. Attempts were made to formulate this method for use without an observed absorption field using an empirically derived ratio of a_{CDOM} to the sum of a_{wat} and a_{phy} , but it produced similar results as the chl-a based approach in equation 2.9. Another effort was made following Baird (2010) by estimating a_{CDOM} as a function of salinity but this, again, underestimated a_{CDOM} at similar values of the chl-a based method. While the chl-a method (and others) underestimated a_{CDOM} at the OOI CE02SHSP site,

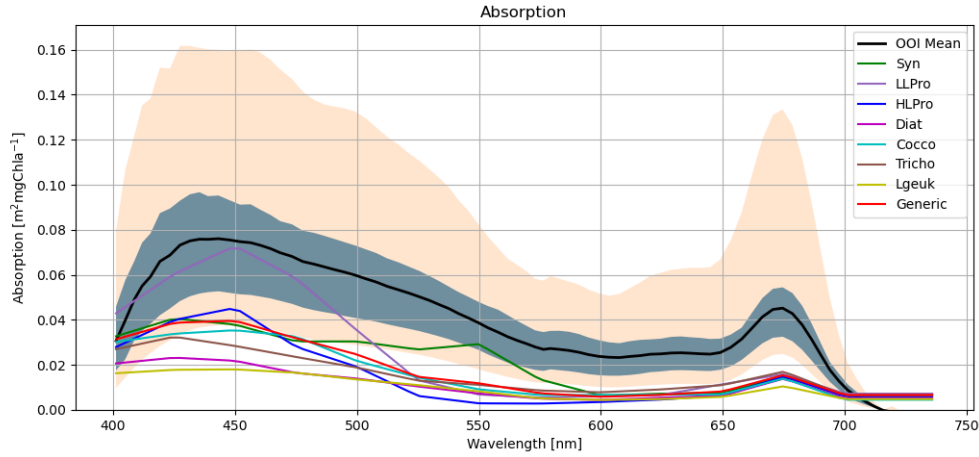


Figure 3.11: α_{phy} (colored lines) compared to $\bar{\alpha}_{\text{OOI}}$ (black line), 20%-80% quantiles (grey shading), and extrema (tan shading). Modeled absorption here is computed using the updated reference absorption based algorithm in equation 3.5.

they all provide an important improvement over not including CDOM at all. Motivated by the possible underestimation of CDOM at OOI CE02SHSP the sensitivity of the CalCOFI and CCI validation to CDOM levels was tested.

CCI and CalCOFI CDOM Sensitivity

In section 3.1 it was shown that using CDOM from equation 2.9 decreased mean R_{rs} RMSRE deviation across wavelengths and phytoplankton types by 10.1% from 160.7% with no CDOM to 144.52% with CDOM. After finding that CDOM was underestimated at OOI CE02SHSP site, the sensitivity of the CalCOFI and CCI R_{rs} model correlation was tested with increased CDOM absorption levels. The average RMSRE results from these tests are provided in table 3.1. It is apparent from the results that increasing CDOM levels provides improvement to mean RMSRE correlation to a limit. This shows that modeled CDOM absorption is likely being underestimated in the CalCOFI domain as well as at OOI CE02SHSP.

CDOM Level	Mean RMSRE (All Wavelengths and All Types)
0a _{CDOM}	160.7%
a _{CDOM}	144.5 %
3a _{CDOM}	129.3 %
6a _{CDOM}	121.1 %
12a _{CDOM}	117.3 %
24a _{CDOM}	119.2 %

Table 3.1: The sensitivity of modeled mean R_{rs} RMSRE across wavelengths and phytoplankton types for the CCI and CalCOFI validation data.

Summary

There are two main takeaways from these results, noting that results are in the context of OOI site CE02SHSP. The first is that current modeled scattering fields correlate well with observations but could further benefit from dynamic community estimates. The second is that modeled absorption fields significantly underestimate observed absorption. This is shown to primarily result from the underestimation of absorption due to CDOM, but other unresolved constituents likely impact the underestimation as well.

Overall, it has been shown that the absorption and scattering estimation stage of the optical model is highly prone to error as a result of the difficulties resolving important optical constituents and dynamic phytoplankton community structure. In order to properly test other two subsequent stages of the model, it is necessary to remove the inherent uncertainty in the first absorption and scattering estimation stage. This can be achieved by modeling the light field with OOI observed

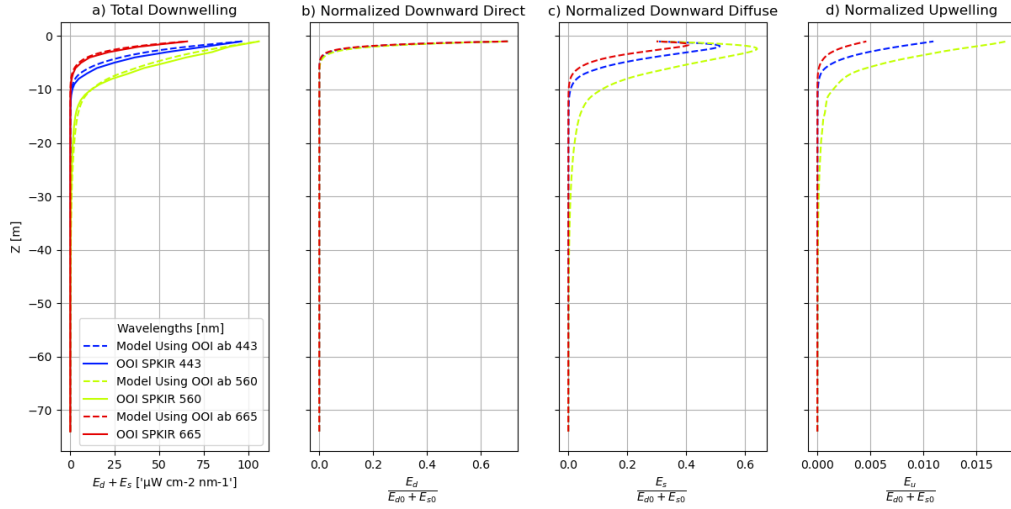


Figure 3.12: a) Profile comparing observed and modeled downwelling irradiance, $E_d + E_s$. The modeled irradiance fields are shown as dashed lines and the observed irradiance field is shown as solid lines. Different wavelengths are plotted with colors corresponding to their wavelength. b) Normalized E_d stream from model. c) Normalized E_s stream from model. d) Normalized E_u stream from model.

absorption and scattering profiles as performed in the following section.

3.2.3 Spectral Irradiance

Using OOI observed total absorption and scattering, a_{OOI} and b_{OOI} , as input into the optical model we can compare the modeled downward irradiance $E_{(d+s)}(a_{\text{OOI}}, b_{\text{OOI}})$ directly to OOI in situ measured downward irradiance, $E_{(d+s)\text{OOI}}$. Using a_{OOI} and b_{OOI} essentially skips the estimates of the first stage of the optical model, thereby giving confidence that the resulting irradiance discrepancies are influenced by irradiance model imperfections only. The comparison of $E_{(d+s)}(a_{\text{OOI}}, b_{\text{OOI}})$ to $E_{(d+s)\text{OOI}}$ is used to validate our implementation of the three stream model and its accuracy in solving for the downward streams.

It is important to note that we add back the effects of water into a_{OOI} and b_{OOI} . The $b_{b_{\text{OOI}}}$ is not explicitly observed, therefore it must be solved for. In order to avoid assuming a phytoplankton type for $b_{b_{\text{OOI}}}$ which is necessary when using an ESD approach as in equation 2.8, we follow Morel et al. (2002) and assume backscatter as a function of chl-a in the following manner,

$$b_{b_{\text{OOI}}} = b_{b_w} + b_{\text{OOI}} [0.002 + (0.01(0.5 - 0.25 \log_{10}(\text{Chl}_{\text{OOI}})))] . \quad (3.7)$$

This approach produces $b_{b_{\text{OOI}}}$ similar in value as the ESD method but with chl-a dependence instead of ESD.

Only two of the three streams are directly validated because OOI SPKIR measures the downward irradiance, but not upwelling. This being said, the coupling of E_s and E_u in the three stream model means that the E_u solution indirectly influences the comparison. Finally, the model is solved using OOI downward irradiance at the surface as the initial value instead of the normalized irradiances previously used, see section 2.3. The ratio of E_{s0}/E_{d0} used remains the same ($E_{d0} = 0.7$ and $E_{s0} = 0.3$).

Figure 3.12 shows a downward irradiance profile comparison between the solution of the optical model, $E_{(d+s)}(a_{\text{OOI}}, b_{\text{OOI}})$, and the irradiance observed by OOI, $E_{(d+s)\text{OOI}}$, for wavelengths 443, 560, and 665. For each wavelength $E_{(d+s)}(a_{\text{OOI}}, b_{\text{OOI}})$ agrees well with $E_{(d+s)\text{OOI}}$. Modeled irradiance at 443nm shows the most deviation from observations. The normalized E_u from model is shown in 3.12.d (separate normalized downwelling streams E_d and E_s are shown in 3.12.b and 3.12.c respectively).

The profile comparison between $E_{(d+s)\text{OOI}}$, $E_{(d+s)}(a_{\text{OOI}}, b_{\text{OOI}})$, and model irradiance using modeled absorption and scattering (single phytoplankton type and chl-a based CDOM estimates), $E_{(d+s)}(a, b)$, is shown in figure 3.13. $E_{(d+s)}(a, b)$

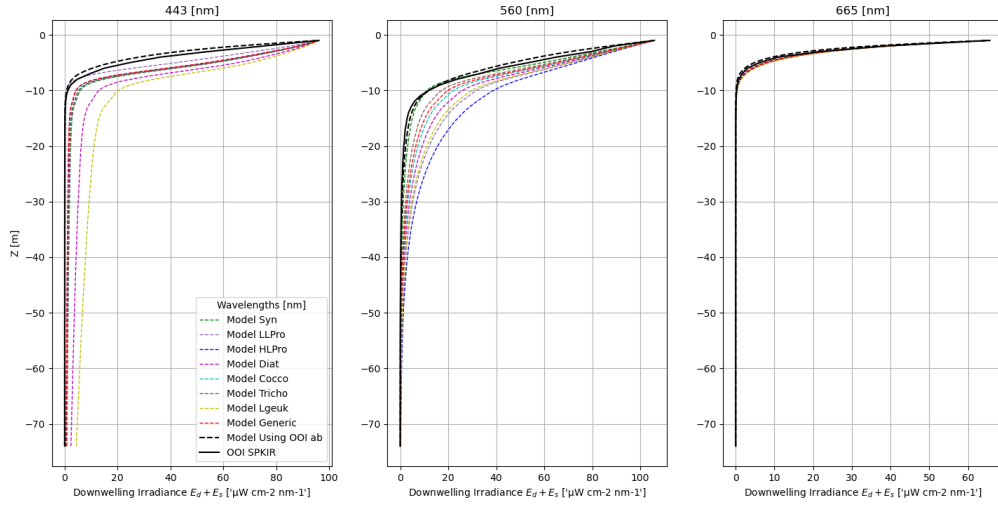


Figure 3.13: The profiles of downward irradiance computed in different ways. The black line corresponds to the measured OOI irradiance. The black dashed line shows the modeled downward irradiance using OOI observed absorption and scattering for input. The colored dashed lines show the model result using modeled absorption and scattering from chl-a profiles. Each color dashed line corresponds to a different phytoplankton type in the legend. Three different wavelengths are plotted including 443 nm (left), 560 nm (center), and 665 nm (right).

shows significantly larger irradiance at depth than both $E_{(d+s)_{\text{OOI}}}$ and $E_{(d+s)}(a_{\text{OOI}}, b_{\text{OOI}})$ for wavelengths 443 nm and 560 nm and for all phytoplankton types. This agrees with the observed underestimation of modeled absorption in section 3.2.2. The relationship between underestimated absorption leading to over estimated irradiance is apparent from the equation 2.1 where a decrease in absorption subsequently decreases the decay rate of the E_d . For 665 nm the modeled absorption and scattering fields correlate well with the observed irradiance. This correlation at 665 nm is thought to result from the domination of absorption due to water at long wavelengths (Nelson & Siegel, 2013). The dominance of water at 665 nm decreases the

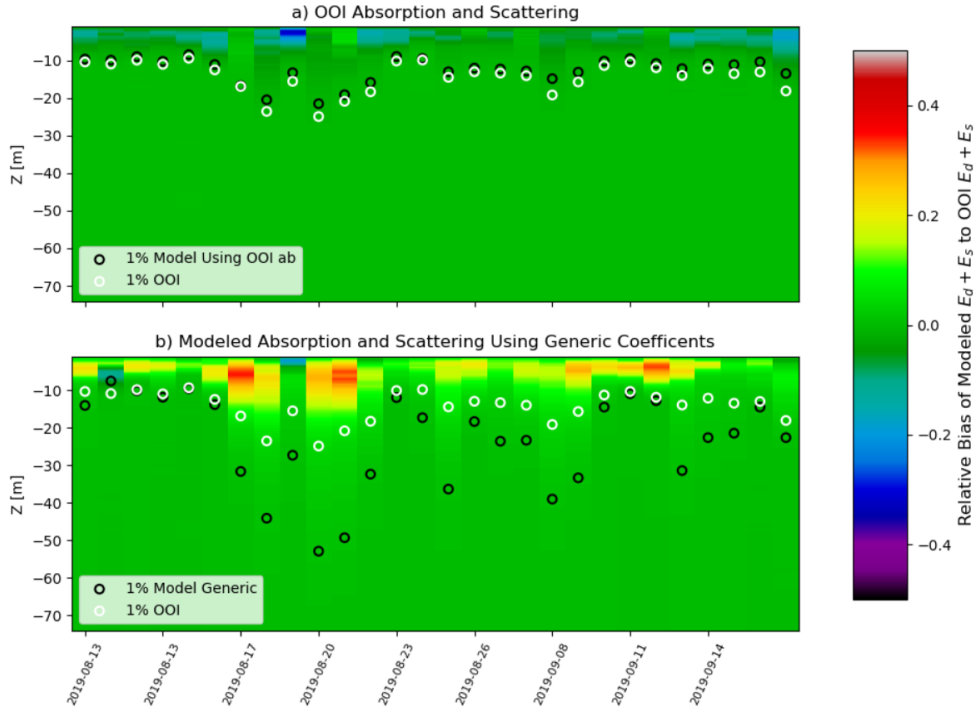


Figure 3.14: a) Relative bias between $E_{(d+s)_{OOI}}$ and $E_{(d+s)}(a_{OOI}, b_{OOI})$. The black circles represent the 1% light level for $E_{(d+s)}(a_{OOI}, b_{OOI})$ and the white circles represent the 1% light level for $E_{(d+s)_{OOI}}$ b) Relative bias between $E_{(d+s)_{OOI}}$ and $E_{(d+s)}(a, b)$ for generic coefficients. The black circles represent the 1% light level for $E_{(d+s)}(a, b)$ and the white circles represent the 1% light level for $E_{(d+s)_{OOI}}$

influence of inaccuracies in estimated constituent absorption and hence the correlation of $E_{(d+s)}(a, b)$ to both $E_{(d+s)_{OOI}}$ and $E_{(d+s)}(a_{OOI}, b_{OOI})$ at 665 nm.

In figure [3.14](#)a we show a time series validation of the model by computing the relative bias between $E_{(d+s)}(a_{OOI}, b_{OOI})$ and $E_{(d+s)_{OOI}}$. Figure [3.14](#)a shows a similar time series but with the relative bias between $E_{(d+s)}(a, b)$ and $E_{(d+s)_{OOI}}$, with $E_{(d+s)}(a, b)$ calculated using the generic phytoplankton type (recall this is the mean absorption of all other types at every wavelength). Both figures show the correspondence of the modeled and observed euphotic zone (1% light level) positions

for each profile in the time series. For both plots, the relative bias is highest in the upper-most 20m which corresponds to the high irradiance dynamics in that portion of the vertical domain.

Figure 3.14a shows that $E_{(d+s)}(a_{\text{OOI}}, b_{\text{OOI}})$ accurately solves the downward irradiance field with the maximum discrepancy from $E_{(d+s)\text{OOI}}$ less than 20% all profiles except one which shows a -30% relative bias. $E_{(d+s)}(a_{\text{OOI}}, b_{\text{OOI}})$ tends to underestimate downward irradiance with this systemic error designated by the negative bias found in 92% of profiles. The 1% light level for $E_{(d+s)}(a_{\text{OOI}}, b_{\text{OOI}})$ and $E_{(d+s)\text{OOI}}$ correlate considerably well with less than 2 m difference in vertical position across profiles. The model underestimates the magnitude of the 1% light level as a result of an underestimated downward irradiance field with 1.7 m mean difference across profiles.

On the other hand 3.14b shows comparatively large deviations of $E_{(d+s)}(a, b)$ from $E_{(d+s)\text{OOI}}$. The relative bias from observations ranges from a 20%-40% maximum for 67% of profiles. $E_{(d+s)}(a, b)$ overestimates the downward irradiance field across the deployment. The significance of this overestimation is well illustrated by the large differences in euphotic zone positions. The mean difference in 1% light level between $E_{(d+s)}(a, b)$ from $E_{(d+s)\text{OOI}}$ is -9.34 m.

It is clear from these results and a qualitative analysis of figure 3.14 that the optical model using observed absorption and scattering produces accurate solutions of downward direct irradiance. It was also shown that using single phytoplankton type and chl-a formulated CDOM based absorption and scattering estimations as input produced significantly less accurate results.

4

Conclusions

The main purpose of this work was to formulate, implement, and test the forward modeling of a radiative transfer model in the ocean to determine its potential for biogeochemical data assimilation of remote sensing reflectance data, $R_{rs}(\lambda)$, in the CCS. It was shown that the optical model can be separated into three distinct stages: estimation of absorption and scattering from observations and parametrizations of optically important constituents, solving the radiative transfer equations, and translating the resulting irradiance field to R_{rs} and chl-a. The implemented methods for each stage were described in detail in chapter 2. This included the implementation of a three-stream irradiance model to solve constituent-dependent irradiance fields using two different numerical methods which are compared to an analytical solution (derived under the assumption of constant absorption and scattering). The shooting up method using a logarithmic and H_A dependent vertical grid was found to be the best numerical approach due to its computational efficiency, ease of implementation, comparable accuracy, and adaptability. The ratio of the resulting downward and upward streams can be translated into R_{rs} for comparison

with satellite data using methods well supported by literature.

After formulating and implementing the optical model, it was tested using CalCOFI cast in situ input data to compare modeled R_{rs} to CCI satellite observations. These comparisons aim to validate all three stages of the model at once. In effort to separate and validate the first two of the three stages individually, OOI profiler data from the CE02SHSP site was also used.

The validation results and subsequent conclusions are addressed in the order that they occur in the optical model—starting with absorption and scattering, and ending with R_{rs} . OOI profiler data showed that observed scattering is on the same order of magnitude as most modeled phytoplankton types, but model estimates significantly underestimate absorption at site CE02SHSP. The underestimation of absorption is found, at least in part, to result from the underestimation of modeled CDOM. Through a set of CDOM sensitivity tests it was also shown that CDOM is likely underestimated in modeled absorption of CalCOFI cast data as well. While the chl-a based CDOM formulation in equation 2.9 tends to underestimate CDOM in these two cases, it still offers improvement to results without CDOM. R_{rs} results are highly sensitive to the choice of phytoplankton type and a type-dependent directional bias suggests that more accurate representations of phytoplankton community structure could improve absorption and scattering estimations and overall model results.

The irradiance model produced accurate downward irradiance fields when using OOI-observed absorption and scattering profiles, giving confidence in the model equations and the numerical implementation. Irradiance fields produced with estimated (rather than observed) absorption and scattering demonstrate significantly less accurate results. Therefore, correctly estimated absorption and scattering fields

are the primary predictor of optical model accuracy.

Assuming single phytoplankton type chl-a the optical model produces R_{rs} values that correlate well with satellite-observed R_{rs} for certain phytoplankton types and poorly for others. Modeled chl-a shows better agreement with in situ chl-a than with satellite-derived chl-a. However, disagreement of the model to both in situ and satellite chl-a suggests that there are inaccuracies in the modeled ratio of blue to green R_{rs} input to the OCx algorithm. This is potentially a result an imperfect directional-dependence of surface irradiance, i.e., unresolved variation in E_{s0}/E_{d0} from atmospheric influences. In situ surface chl-a to satellite chl-a observations did not correlate well, which illustrates a broader challenge of relating satellite remote sensing estimates with in situ values (e.g., due to mismatch in satellite averaging scales with small-scale phytoplankton variability in the ocean). Using the fact that optical model accuracy is primarily dependent on absorption and scattering, I argue that R_{rs} accuracy can be improved with community structure and enhanced CDOM estimations. If absorption and scattering issues are resolved, I believe that the optical model can be used for data assimilation of R_{rs} in confidence that it will reflect R_{rs} response to dynamic community structure the same or better than the surface chl-a based approach.

4.1 Moving forward

It was shown that accurate representation of the absorption and scattering fields is the primary predictor of optical model accuracy. Therefore, the most immediately achievable improvement to the optical model is more accurately resolving the absorption and scattering of the modeled water column. This includes properly

resolving community structure, formulation of accurate CDOM estimates, inclusion of detritus, the possible addition of other optically important phytoplankton types, and ensuring that coefficients of absorption and scattering for currently used types are accurate.

I induced that improved absorption and scattering estimates would improve R_{rs} correlation to satellite. Future work should explicitly test if this is the case. This could be achieved through the use of observed absorption and scattering profiles and comparing the resulting R_{rs} to satellite. This was attempted with OOI deployment 15, but very few (less than 5) profiles were matched to a satellite observation. This is thought to be the result of the significant cloud cover of coastal Oregon. Further work might seek OOI validation data over many deployments.

A better estimation of the variability of the diffuse and downward direct ratio on wavelength and atmospheric conditions could also provide important improvements to the model. This could be achieved with optical model coupling to a atmospheric model, or even a parametrization of the general relationship of the directional ratio to wavelength would be an improvement.

Implementation of oligotrophic style ocean color algorithm for the derivation of low level chl-a concentrations from R_{rs} is another possible inclusion, although it would only aid chl-a estimates not R_{rs} , see [Hu et al. \(2012\)](#).

Once the above steps have been taken, the optical light model could be adopted for the biogeochemical model assimilation of R_{rs} data.

Bibliography

- Aas, E. (1987). Two-stream irradiance model for deep waters. *Applied Optics*, 26(11), 2095–2101.
- Baird, M. E. (2010). Limits to prediction in a size-resolved pelagic ecosystem model. *Journal of Plankton Research*, 32(8), 1131–1146.
- Baird, M. E., Cherukuru, N., Jones, E., Margvelshvili, N., Mongin, M., Oubelkheir, K., Ralph, P. J., Rizwi, F., Robson, B. J., Schroeder, T., Skeratt, J., Steven, A. D., & Wild-Allen, K. A. (2016). Remote-sensing reflectance and true colour produced by a coupled hydrodynamic, optical, sediment, biogeochemical model of the great barrier reef, australia: Comparison with satellite data. *Environmental Modelling and Software*, 78, 79–96.
- Dutkiewicz, S., Hickman, A. E., & Jahn, O. (2018). Modeling ocean-colour-derived chlorophyll a. *Biogeosciences*, 15, 613–630.
- Dutkiewicz, S., Hickman, A. E., Jahn, O., Gregg, W. W., Mouw, C. B., & Follows, M. J. (2015). Capturing optically important constituents and properties in a marine biogeochemical and ecosystem model. *Biogeosciences*, 12, 4447–4481.
- Edwards, C. A., Moore, A. M., Hoteit, I., & Cornuelle, B. D. (2015). Regional ocean data assimilation. *Annu. Rev. Mar. Sci.*, 7, 21–42.

- Fennel, K., Gehlen, M., Brasseur, P., Brown, C. W., Ciavatta, S., Cossarini, G., Crise, A., Edwards, C. A., Ford, D., Friedrichs, M. A. M., Gregoire, M., Jones, E., Kim4, H.-C., Lamouroux, J., Murtugudde, R., & Perruche, C. (2019). Advancing marine biogeochemical and ecosystem reanalyses and forecasts as tools for monitoring and managing ecosystem health. *Front. Mar. Sci.*, 6(89), 2016–2040.
- Gregg, W. W. & Casey, N. W. (2009). Skill assessment of a spectral ocean - atmosphere radiative model. *Journal of Marine Systems*, 76, 49–63.
- Gregg, W. W. & Rousseaux, C. S. (2016). Directional and spectral irradiance in ocean models: Effects on simulated global phytoplankton, nutrients, and primary production. *Front. Mar. Sci.*, 3(240), 1–19.
- Gregg, W. W. & Rousseaux, C. S. (2017). Simulating pace global ocean radiances. *Front. Mar. Sci.*
- Hu, C., Lee, Z., & Franz, B. (2012). Chlorophyll-a algorithms for oligotrophic oceans: A novel approach based on three-band reflectance difference. *Journal of Geophysical Research*, 117(C1).
- Jones, E. M., Baird, M. E., Mongin, M., Parslow, J., Skerratt, J., Lovell, J., Margvelashvili, N., Matear, R. J., Wild-Allen, K., Robson, B., Rizwi, F., Oke, P., King, E., Schroeder, T., Steven, A., & Taylor, J. (2016). Use of remote-sensing reflectance to constrain a data assimilating marine biogeochemical model of the great barrier reef. *Biogeosciences*, 13, 6441–6469.
- Jouini, M., Levy, M., Crepon, M., & Thiria, S. (2013). Reconstruction of satellite chlorophyll images under heavy cloud coverage using a neural classification method. *Remote Sensing of Environment*, 131, 232–246.

- Kishi, M. J., Kashiwai, M., Ware, D. M., Megreye, B. A., Eslinger, D. L., Werner, F. E., Noguchi-Aitab, M., Azumaya, T., Fujij, M., Hashimoto, S., Huangl, D., Iizumi, H., Ishidav, Y., Kango, S., Kantakovp, G. A., cheol Kimo, H., Komatsun, K., Navrotsky, V. V., Smithb, S. L., Tadokoro, K., Tsuda, A., Yamamura, O., Yamanakai, Y., Yokouchi, K., Yoshiei, N., Zhangt, J., Zuenko, Y. I., & Zvalinsky, V. I. (2007). Nemuro—a lower trophic level model for the north pacific marine ecosystem. *Ecological Modeling*, 202, 12–25.
- Kitidis, V., Stubbins, A. P., Uher, G., Goddard, R. C., Law, C. S., & Woodward, E. M. S. (2013). The global distribution and dynamics of chromophoric dissolved organic matter. *Annu. Rev. Mar. Sci*, 5, 447–476.
- Kylling, A., Stamnes, K., & Tsay, S. C. (1995). A reliable and efficient two-stream algorithm for spherical radiative transfer: Documentation of accuracy in realistic layered media. *Journal of Atmospheric Chemistry*, 21, 115–150.
- Lee, Z., Carder, K. L., & Arnone, R. A. (2002). Deriving inherent optical properties from water color: a meltiband quasi-analytical algorithm for optically deep waters. *Applied Optics*, 41(27), 5755–5772.
- Lee, Z., Weidemann, A., Kindle, J., Arnone, R., Carder, K. L., & Davis, C. (2007). Euphotic zone depth: Its derivation and implication to ocean-color remote sensing. *Journal of Geophysical Research*, 112(C3).
- Lorenzen, C. J. (1972). Extinction of light in the ocean by phytoplankton. *J. Cons. Int. Explor. Mer.*, 34(2), 262–267.
- Mobley, C. (2021). Measures of reflectance. *Ocean Optics Web Book*.

- Morel, A., Antoine, D., & Gentili, B. (2002). Bidirectional reflectance of oceanic waters: accounting for raman emission and varying particle scattering phase function. *Applied Optics*, 41(30), 6289–6306.
- Morel, A. & Gentili, B. (1993). Diffuse reflectance of oceanic water. ii. bidirectional aspects. *Applied Optics*, 32(33), 6864–6879.
- Nelson, N. B. & Siegel, D. A. (2013). The global distribution and dynamics of chromophoric dissolved organic matter. *Annu. Rev. Mar. Sci.*, 5, 447–476.
- O’Reilly, J. E., Maritorena, S., Mitchell, B. G., Siegel, D. A., Carder, K. L., Garver, S. A., Kahru, M., & McClain, C. (1998). Ocean color chlorophyll algorithms for seawifs. *Journal of Geophysical Research*, 103(C11), 24,937–24,953.
- O’Reilly, J. E., Maritorena, S., O’Brien, M. C., Siegel, D. A., Toole, D., Menzies, D., Smith, R. C., Mueller, J. L., Mitchell, B. G., Kahru, M., Chavez, F. P., Strutton, P., Cota, G. F., Hooker, S. B., McClain, C. R., Carder, K. L., Muller-Karger, F., Harding, L., Magnuson, A., Phinney, D., Moore, G. F., Aiken, J., Arrigo, K. R., Arrigo, R. R., Letelier, R., & Culver, M. (2000). Seawifs post launch calibration and validation analyses, part 3. *Nasa Tech. Memo.*, 11, 1–49.
- Press, W. H., Teukolsky, S. A., Vetterling, W. T., & Flannery, B. P. (2007). Numerical recipes: the art of scientific computing. *Cambridge University Press*, 3, 955–964.
- Quééré, C. L., Harrison, S. P., Prentice, I. C., Buitenhuis, E. T., Aumont, O., Bopp, L., Claustre, H., Cunha, L. C. D., Geider, R., Giraud, X., Klaas, C., Kohfeld, K. E., Legendre, L., Manizza, M., Platt, T., Rivkin, R. B., Sathyendranath, S., Uitz, J., Watson, A. J., & Wolf-Gladrow, D. (2005). Ecosystem dynamics based

- on plankton functional types for global ocean biogeochemistry models. *Global Change Biology*, 11(11), 2016–2040.
- Ryer, A. D. (1997). The light measurement handbook. *International Light, Inc.*, 2, 31–36.
- Sathyendranath, S. & Platt, T. (1997). Analytic model of ocean color. *Applied Optics*, 36(12), 2620–2629.
- Sathyendranath, S. & Platt, T. (1998). Ocean-color model incorporating transspectral processes. *Applied Optics*, 37(12), 2216–2227.
- Song, H., Edwards, C. A., Moore, A. M., & Fiechter, J. (2016). Data assimilation in a coupled physical-biogeochemical model of the california current system using an incremental lognormal 4-dimensional variational approach: Part 3—assimilation in a realistic context using satellite and in situ observations. *Ocean Modeling*, 106, 159–172.
- Stramska, M. & Stramski, D. (2005). Effects of a nonuniform vertical profile of chlorophyll concentration on remote-sensing reflectance of the ocean. *Applied Optics*, 44(9), 1735–1747.
- Toon, O. B., Mckay, C. P., & Ackerman, T. P. (1989). Rapid calculation of radiative heating rates and photodissociation rates in inhomogenous multiple scattering atmospheres. *Journal of Geophysical Research*, 94(D13), 16,287–16,301.
- Venturi, D. (2022). Numerical methods to solve boundary value problems for odes. *AM 213B Course Notes, University of California Santa Cruz*, 1(1), 1–18.
- Wald, L. (2018). Basics in solar radiation at earth surface. *HAL*, (pp.53).

Werdell, P. J. & Bailey, S. W. (2005). An improved in-situ bio-optical data set for ocean color algorithm development and satellite data product validation. *Remote Sensing of Environment*, 98(1), 122–140.

Whitmire, A. L., Pegau, W. S., Karp-Boss, L., Boss, E., & Cowles, T. J. (2010). Spectral backscattering properties of marine phytoplankton cultures. *Optics Express*, 18(14), 15073–15093.